OMI/Aura Nitrogen Dioxide Standard Product Version 4.0 with Improved Surface and Cloud Treatments

Lok N. Lamsal [*,1,2], Nickolay A. Krotkov[2], Alexander Vasilkov[2,3], Sergey Marchenko[2,3], Wenhan Qin[2,3], Eun-Su Yang[2,3], Zachary Fasnacht[2,3], Joanna Joiner[2], Sungyeon Choi[2,3], David Haffner[2,3], William H. Swartz[4], Bradford Fisher[2,3], Eric Bucsela[5]

[1]University Space Research Association, Greenbelt, MD 20770, USA

[2]NASA Goddard Space Flight Center, Greenbelt, MD 20770, USA

[3]Science Systems and Applications, Lanham, MD 20706, USA

[4]Johns Hopkins University, Applied Physics Laboratory, Laurel, MD 20723, USA

[5]SRI International, Menlo Park, CA 94025, USA

[*]Corresponding author: Email: lok.lamsal@nasa.gov.

Abstract

We present a new and improved version (V4.0) of the NASA standard nitrogen dioxide (NO_2) product from the Ozone Monitoring Instrument (OMI) on the Aura satellite. This version incorporates the most salient improvements for OMI NO_2 products suggested by expert users and enhances the NO_2 data quality in several ways through improvements to the air mass factors (AMFs) used in the retrieval algorithm. The algorithm is based on geometry-dependent surface Lambertian equivalent reflectivity (GLER) operational product that is available on an OMI pixel basis. GLER is calculated using the vector linearized discrete ordinate radiative transfer (VLIDORT) model, which uses as input high resolution bidirectional reflectance distribution function (BRDF) information from NASA's Aqua Moderate Resolution Imaging Spectroradiometer (MODIS) instruments over land and the wind-dependent Cox–Munk wave-facet slope distribution over water, the latter with contribution from the water-leaving radiance. The GLER combined with consistently retrieved oxygen dimer (O_2-O_2) absorption-based effective cloud fraction (ECF) and optical centroid pressure (OCP) provide improved information to the new NO_2 AMF calculations. The new AMFs increase the retrieved tropospheric NO_2 by up to 50% in highly polluted areas; these differences arise from both cloud and surface BRDF effects as well as biases between the new MODIS-based and previously used OMI-based climatological surface reflectance data sets. We quantitatively evaluate the new NO_2 product using independent observations from ground-based and airborne instruments. The new V4.0 data and relevant explanatory documentation are publicly available from the NASA Goddard Earth Sciences Data and Information Services Center (https://disc.gsfc.nasa.gov/datasets/OMNO2_V003/summary/), and we encourage their use over previous versions of OMI NO_2 products.

Introduction

The Dutch/Finnish-built Ozone Monitoring Instrument (OMI) has been operating on board the NASA EOS-Aura spacecraft since July 2004 (Levelt et al., 2006, 2018). The primary objectives of OMI's mission are to continue the long-term record of total column ozone and to monitor other trace gases relevant to tropospheric pollution worldwide. Observations of sunlight backscattered from the Earth over a wide range of UV and visible wavelengths (~260-500 nm) made by OMI allow for the retrieval of various atmospheric trace gases, including nitrogen dioxide (NO_2). NO_2 is a critically important short-lived air pollutant originating from both anthropogenic and natural sources. It is the principal precursor to tropospheric ozone and a key agent for the formation of several toxic airborne substances such as nitric acid (HNO_3), nitrate aerosols, and peroxyacetyl nitrate. Satellite-based observations yield a global, self-consistent NO_2 data record that can complement field measurements.

During more than 16 years of operation, OMI has provided a unique, practically uninterrupted daily NO_2 data record that has been widely used for atmospheric research and applications, accentuating demands for accurate NO_2 data products. The power of OMI to track NO_2 pollution is demonstrated through observations of enhanced column amounts over polluted industrial areas (*e.g.*, Boersma et al., 2011; Lamsal et al., 2013; Krotkov et al., 2016; Kim et al., 2016; Cai et al., 2018; Montgomery and Halloway, 2018), weekly patterns with significant reduction on weekends following energy usage (*e.g.*, Ialongo et al., 2016), and seasonal patterns (e.g., van der A et al., 2008) that reflect changes in NO_x emissions and photochemistry (*e.g.*, Shah et al., 2019). Exploiting the close relationship between NO_x emissions and tropospheric NO_2 columns, OMI NO_2 data have been used to detect and quantify the strength and trends of NO_x emissions from power plants (Duncan et al., 2013; de Foy *et al.*, 2015; Liu et al., 2019), ships (*e.g.*, Vinken et al., 2014a), lightning (*e.g.*, Picketing et al., 2016), soil (*e.g.*, Vinken et al., 2014b), oil and gas production (e.g., Dix et al., 2020), forest fires (Schreier et al, 2014), and other area sources such as cities in the US (Lamsal *et al.,* 2015; Lu *et al.,* 2015; Kim et al., 2016), Europe (*e.g.*, Zhou et al., 2012; Castellanos et al., 2012; Vinken et al., 14a), Asia (Ghude et al., 2013; Goldberg et al., 2019a), and other world urban areas (Krotkov *et al.,* 2016; Duncan *et al.*, 2016; Montgomery and Halloway, 2018). OMI NO_2 observations have frequently seen used to evaluate chemical transport models (CTMs) (*e.g.*, Herron-Thrope et al., 2010; Han et al., 2011; Hudman et al., 2012; Pope et al., 2015; Rasool et al., 2016), to study atmospheric NO_x chemistry and lifetime (*e.g.*, Lamsal et

71 al., 2010; Beirle et al., 2011; Canty et al., 2015; Tang et al., 2015; Laughner and Cohen, 2019),
72 and to infer ground-level NO_2 concentrations (Lamsal et al., 2008; Gu et al., 2017), NO_2 dry
73 deposition (Nowlan et al., 2014, Geddes and Martin, 2017), and emissions of co-emitted gases
74 including carbon dioxide (CO_2) (Konovalov et al., 2016; Goldberg et al., 2019b, Liu et al., 2019).

75 Over the last decade, there have been considerable efforts to improve NO_2 data quality from OMI
76 and other satellite instruments (e.g., Boersma et al., 2018). A special emphasis has been placed on
77 improving auxiliary information (e.g., a priori NO_2 vertical profiles, surface reflectivity),
78 particularly with respect to spatial and temporal resolution. For instance, the global OMI NO_2
79 products are based on a priori NO_2 profiles from relatively coarse-resolution ($>1.0°× 1.25°$) global
80 CTM simulations (Boersma et al., 2011; Krotkov et al., 2017, Choi et al., 2020). Many regional
81 studies suggest a general low-bias in the global tropospheric NO_2 column products, particularly
82 over polluted areas, that can be partially mitigated by using a-priori information from high-
83 resolution CTM simulations (Russell et al., 2011, McLinden et al., 2014; Lin et al., 2014; 2015;
84 Goldberg et al., 2018; Choi et al., 2020). Current global NO_2 retrievals are based on a low-
85 resolution ($0.5°× 0.5°$) static climatology of surface Lambert-Equivalent Reflectivity (OMLER)
86 product (Kleipool et al., 2008), which is likely biased high due to insufficient cloud and aerosol
87 screening. This bias in surface reflectivity can lead to an underestimation of tropospheric NO_2
88 retrievals (Zhou et al., 2010; Lin et al., 2014; Vasilkov et al., 2017). In addition, the OMLER data
89 do not account for the significant day-to-day (orbital) variability in surface reflectance caused by
90 changes in sun-satellite geometry, a phenomenon often expressed by the bi-directional reflectance
91 distribution function (BRDF). Zhou et al. (2010) demonstrated the impact of both the spatial
92 resolution and the BRDF effect on OMI tropospheric NO_2 retrievals over Europe by using high-
93 resolution surface BRDF and albedo products from the Moderate Resolution Imaging
94 Spectroradiometer (MODIS). Taking advantage of the MODIS high resolution data, albeit
95 neglecting the BRDF and atmospheric effects, Russell et al (2011) and McLinden et al (2014)
96 created improved NO_2 products from the NASA Standard Product (Bucsela et al., 2013; Lamsal
97 et al., 2014) over the continental US and Canada, respectively. While these and subsequent studies
98 (e.g., Kuhlmann et al., 2015; Laughner et al., 2019) addressed the limitation of climatological LER
99 data on NO_2 retrievals, they did not account for the surface BRDF effect on the OMI cloud products
100 (cloud pressure/fraction), which are also inputs to the NO_2 algorithm. Applying the MODIS BRDF
101 data consistently to both the NO_2 and cloud retrievals demonstrably improves the quality of OMI

102   NO₂ retrievals over China (Lin et al., 2014, 2015, Liu et al., 2019). However, this approach is

103   computationally expensive and is applicable to land surfaces only. Our previous work (Vasilkov

104   et al., 2018) proposed an approach appropriate for satellite NO₂ data processing on a global scale

105   (a) by using MODIS BRDF information consistently in the cloud and NO₂ retrievals; (b) for both

106   land and water; and (c) in an efficient way. Here, we apply the approach globally for the first time

107   in the standard NASA OMI NO₂ algorithm.

108   In this paper we describe various updates made in the version 4.0 (V4.0) NASA OMI NO₂

109   algorithm, discuss their impact on the retrievals of tropospheric and stratospheric NO₂ column

110   amounts, and provide an initial quantitative assessment of NO₂ data quality. Section 2 describes

111   the OMI NO₂ algorithm and various auxiliary data used by the algorithm. We present validation

112   results in Section 3. Section 4 summarizes the conclusions of this study.

113   **2 OMI and the NO₂ Standard Product**

114   OMI is a ultraviolet-visible (UV-Vis) spectrometer on the polar-orbiting NASA Aura satellite

115   (Levelt et al., 2006, 2018). Aura, launched on July 15, 2004, follows a sun-synchronous orbit with

116   an equator crossing time near 13:45 local time. OMI employs two-dimensional CCD detectors and

117   operates in a push-broom mode, registering spectral data over a 2600 km cross-track spatial swath.

118   The broad swath enables global daily coverage within 14-15 orbits. In the OMI visible channel

119   used for NO₂ retrievals, each swath, measured every two seconds, comprises 60 cross-track fields

120   of view (FOVs) varying in size from ~13 km × 24 km near nadir to ~24 km × 160 km for the FOVs

121   at the outermost edges of the swath. Each orbit consists of ~1650 swaths from terminator to

122   terminator. OMI's full daily coverage has been affected by data loss due to an anomaly presumably

123   caused by material on the spacecraft outside the instrument that results in reduced coverage to

124   about half of its original swath as discussed in Section 2.4.

125   The OMI NO₂ Standard Product (OMNO2) algorithm provides retrievals of NO₂ column (total,

126   tropospheric, and stratospheric) amounts by exploiting Level-1B calibrated radiance and irradiance

127   data from the Vis channel (350-500 nm with 0.63 nm spectral resolution). The algorithm employs

128   a multi-step procedure that consists of 1) a spectral fitting algorithm to calculate NO₂ slant column

129   densities (SCDs) as discussed in Section 2.1; 2) determination of air mass factors (AMFs) to

130   convert SCDs to vertical column densities (VCDs) as discussed in detail in Section 2.2; 3) a

131   scheme to remove cross-track dependent artifacts or stripes; and 4) a stratosphere-troposphere

132   separation scheme to derive tropospheric and stratospheric NO₂ VCDs. The AMF depends upon a

133   number of parameters including optical geometry (solar and viewing azimuth and zenith angles),

134   surface reflectivity, cloud pressure and fraction, and the shape of the NO_2 a priori vertical profile.

135   Since the first release of OMNO2 in 2006 (Bucsela et al., 2006; Celarier et al., 2008), there have

136   been significant conceptual and technical improvements in the retrieval of NO_2 from space-based

137   measurements. Prior versions developed a new scheme for separating stratospheric and

138   tropospheric components in version 2.1 (V2.1) (Bucsela et al., 2013, Lamsal et al., 2014) and a

139   new algorithm for improved NO_2 SCD retrievals in V3.0 (Marchenko et al., 2015, Krotkov et al.,

140   2017), and included improved cloud products (Veefkind et al., 2016) in V3.1 (Choi et al., 2020).

141   The current version, V4.0, further improves on the retrievals in a number of significant ways for

142   NO_2 AMF and VCD calculations. Figure 1 shows a schematic diagram of the retrieval algorithm,

143   and Table 1 summarizes the differences and similarities between previous (V3.1) and current (V4)

144   versions. Some of the approaches in the V4 algorithm are similar to those used in V3.1, but there

145   are several important changes as discussed in detail in Sections 2.1 and 2.2.

146   **2.1 NO_2 and O_2-O_2 spectral fitting**

147   **2.1.1 NO_2 spectral fitting algorithm**

148   The spectral fitting algorithm for the operational standard OMI NO_2 product is described in detail

149   in Marchenko et al. (2015). Briefly, the algorithm retrieves NO_2 slant column densities (SCDs) by

150   using a Differential Optical Absorption Spectroscopy (DOAS) approach (e.g., Platt and Stutz,

151   2006). In the DOAS approach, laboratory-measured spectra of NO_2 (Vandaele et al., 1998) and

152   glyoxal (Volkamer et al., 2005), HITRAN08-based water vapor spectra (Rothman et al., 2009),

153   and rotational Raman (RR; Ring effect) filling-in are sequentially fitted to the OMI-measured

154   reflectance spectrum in the 402-465 nm wavelength range. The slant column represents the

155   integrated abundance of NO_2 along the average photon path from the Sun, through the atmosphere,

156   to the satellite. The Ring spectra are calculated as a linear combination of the atmospheric (Joiner

157   et al. 1995) and the liquid-water (Vasilkov et al., 2002) RR spectra, convolved with the wavelength

158   and cross-track dependent OMI transfer function (Dirksen et al., 2006). The algorithm employs a

159   multi-step, iterative retrieval procedure for removal of the Ring and spectral under-sampling

160   (Chance, et al., 2005) patterns as well as a low-order polynomial smoothing prior to estimation of

161   SCDs for all interfering species. This is in contrast with the conventional DOAS approach that

162   treats the Ring effect as a pseudo-absorber and fits all absorbers simultaneously with the

163   polynomial functions. For accurate wavelength shifts (radiances vs. irradiances), the standard
164   product algorithm splits the entire fitting window into seven carefully selected, partially
165   overlapping micro-windows, iteratively evaluates the RR spectrum amplitudes, performs
166   wavelength adjustments for each segment, and then iteratively retrieves the NO_2, H_2O, and glyoxal
167   in the windows best suited for a particular trace-gas species.

168   The OMI NO_2 SCDs from the standard product were compared with improved SCD retrievals
169   from the Quality Assurance for Essential Climate Variables (QA4ECV, http://www.qa4ecv.eu/),
170   BIRA-IASB's (Royal Belgian Institute for Space Aeronomy) QDOAS software (http://uv-
171   vis.aeronomie.be/software/QDOAS/), and the latest KNMI retrievals (van Geffen et al., 2015) and
172   are shown to agree within 2% (Zara et al., 2018). The typical NO_2 SCD uncertainties amount to
173   $\sim 0.8 \times 10^{15}$ molec cm^{-2}, or 5-7% in high-SCD areas and 15-20% in low-SCD values (Marchenko et
174   al., 2015).

175   **2.1.2 O_2-O_2 spectral fitting algorithm**

176   The oxygen dimer (O_2-O_2) slant column fitting algorithm shares many features of the NO_2 fitting
177   algorithm and is described in detail in Vasilkov et al. (2018). It consists of a multi-step, iterative
178   retrieval approach with three carefully selected micro-windows sampling the flanks and the core
179   of the broad O_2-O_2 feature centered at 477 nm. The algorithm exploits OMI-measured reflectance
180   spectra in the 451-496 nm range to determine the wavelength shifts and RR amplitudes. The Ring
181   patterns are removed from the original OMI reflectances during the iterative adjustments for
182   differences in the wavelength registration of radiances and irradiances. The O_2-O_2 slant columns
183   are retrieved after removal of the NO_2 and H_2O absorptions estimated by the algorithm discussed
184   in the previous section, and of the ozone absorption using total ozone data from Veefkind et al.
185   (2006). After removal of the interfering signals, the 477 nm O_2-O_2 absorption profile is carefully
186   normalized to the adjacent O_2-O_2 absorption-free reflectance levels accounting for very different
187   wavelength dependencies of surface reflectances over various geographical sites (e.g., the open-
188   ocean and desert area), as described in Vasilkov et al. (2018). The normalized O_2-O_2 absorption
189   profiles are then iteratively fitted with the temperature-dependent cross-sections from Thalman
190   and Volkamer (2013) over the 463-488 nm range to derive O_2-O_2 SCDs. These are used to estimate
191   the cloud properties as discussed below in Section 2.2.2.

2.2 Improved air mass factor calculations

The AMF, which is defined as the ratio of SCD to VCD, is needed to calculate the retrieved NO_2 VCD. Details of the AMF and its calculation are given in Palmer et al. (2001). The AMF for each FOV is calculated by combining altitude (z)-dependent scattering weights (w) computed with a radiative transfer model and a local a priori vertical NO_2 profile shape (S), taken from a chemistry-transport model:

$$AMF = \int_{z_1}^{z_2} w(z)S(z)dz. \tag{1}$$

For the tropospheric AMF, the integral extends from the surface to the tropopause, whereas the integral from the tropopause to the top of the atmosphere provides the stratospheric AMF. The scattering weight at a given altitude describes the sensitivity of the backscattered radiation to the abundance of the absorber at that altitude. For an optically thin absorber like NO_2, scattering weights are a function of atmospheric scattering and are considered to be independent of the species' vertical distribution (Palmer et al., 2001). Factors affecting scattering weights include wavelength, optical geometry (solar and viewing azimuth and zenith angles), surface reflectivity, and cloud pressure and fraction. The wavelength dependence of scattering weights is accounted for by creating an average of scattering weights derived from the values at multiple wavelengths within the NO_2 spectral fitting window. To compensate for the effect of the assumed constant NO_2 temperature (220 K) in the NO_2 SCD retrievals, the scattering weights are corrected for the atmospheric temperature effect using local climatological monthly temperature profiles as discussed in Bucsela et al. (2013). These profiles are based on the meteorological field from the Modern-Era Retrospective Analysis for Research and Applications (MERRA-2) (Gelaro et al., 2017).

The a priori NO_2 profile shapes are computed from a monthly mean climatology of vertical NO_2 profiles constructed from the Global Modeling Initiative (GMI) CTM simulation (Douglass et al. 2004, Strahan et al., 2007, Strode et al., 2015) driven by MERRA-2 meteorology. The spatial resolution of the model is 1.25° in longitude and 1.0° in latitude, and the atmosphere is divided into 72 pressure levels extending from the surface to 0.01 hPa. The model output is sampled between 13:00 - 14:00, local time, consistent with the OMI overpass time. The use of monthly NO_2 profiles helps capture the seasonal variation in the NO_2 vertical distribution (Lamsal et al., 2010). The simulation is based on yearly varying NO_x emissions, as discussed in Strode et al., (2015); this is necessary to account for the effect of rapidly changing NO_x emissions (e.g., Tong

223   et al., 2015; Duncan et al., 2016; Miyazaki et al., 2017) on local NO_2 profile shapes (Lamsal et al.,

224   2015; Krotkov et al., 2017).

225   For each FOV, AMFs are computed for clear (AMF_{clr}) and cloudy (AMF_{cld}) conditions. The AMF

226   of a partially cloudy scene is calculated by assuming the independent pixel approximation:

227          $AMF = (1 - f_r) \times AMF_{clr} + f_r \times AMF_{cld},$ (2)

228   where f_r is the cloud radiance fraction (CRF), defined as the fraction of the measured radiation

229   that comes from clouds and scattering aerosols, and is computed at 440 nm from the retrieved

230   effective cloud fraction (ECF), f_c using Equation 8 (see below). AMF_{clr} is calculated for the

231   ground reflectivity of R_s and at terrain pressure P_s, whereas AMF_{cld} is calculated assuming a

232   Lambertian surface of reflectivity 0.8 at the retrieved cloud pressure. Below we provide a detailed

233   discussion of each of these input parameters that are incorporated in the OMNO2 V4.0 algorithm.

234   **2.2.1 New surface reflectivity product for NO₂ and cloud retrievals**

235   Surface reflectivity is an important input parameter for UV/Vis satellite retrievals of trace gases

236   and cloud information. The surface reflectance over both ocean and land depend upon viewing and

237   illumination geometry and can be accurately described by the bidirectional reflectance distribution

238   function (BRDF). This effect is, however, neglected by most currently available trace gas and

239   cloud algorithms which use a climatological Lambert-equivalent reflectivity (LER) for the surface.

240   To account for surface BRDF effects in the NO_2 and cloud retrievals, here we use the geometry-

241   dependent surface LER (GLER) product derived using the Moderate Resolution Imaging

242   Spectroradiometer (MODIS) BRDF data and the Vector Linearized Discrete Ordinate Radiative

243   Transfer (VLIDORT) calculation (Vasilkov et al., 2017; Qin et al., 2019; Fasnacht et al., 2019).

244   The GLER allows for a computationally efficient approach that does not require major changes to

245   the existing trace gas and cloud algorithms.

246   We derive GLER by inverting the top-of-atmosphere (TOA) radiance (*I*) of a Rayleigh atmosphere

247   over a non-Lambertian surface for each specific FOV and Sun-satellite geometry within the

248   Lambertian framework, i.e.,

249          $I = I_0 + GLER \times T/(1 - GLER \times S_b),$ (3)

250   where I_0 is the TOA radiance calculated for a black surface, T is the total (direct + diffuse) solar

251   irradiance reaching the surface converted to the ideal Lambertian-reflected radiance (by dividing

252   by π steradians) and then multiplied by the transmittance of the reflected radiation between the

253 surface and TOA in the direction of a satellite instrument, and S_b is the diffuse flux reflectivity of

254 the atmosphere for the case of its isotropic illumination from below (Dave, 1978). The value of I_0,

255 T, and S_b are pre-computed with VLIDORT and stored in a look-up table. The GLER values are

256 calculated at wavelengths relevant for both NO_2 (440 nm) and cloud (466 nm) retrievals.

257 Over land, the BRDF is calculated using the Ross-Thick Li-Sparse kernel model (Lucht et al.,

258 2000) in VLIDORT (Spurr, 2006):

259 $$BRDF = a_{iso} + a_{vol}k_{vol} + a_{geo}k_{vol}, \tag{4}$$

260 where the coefficients, a_{iso}, a_{vol}, and a_{geo} come from the Moderate Resolution Imaging

261 Spectroradiometer (MODIS) Collection 5 gap-filled, seasonal snow-free BRDF product

262 MCD43GF (Schaaf et al., 2002, 2011) for band 3 (459-479 nm) available at 30 arc-second spatial

263 resolution and 8-day temporal resolution. The term a_{iso} is the isotropic contribution describing the

264 Lambertian part of light reflection from the surface, the volumetric kernel (k_{vol}) describes light

265 reflection from a dense leaf canopy, and the geometric kernel (k_{geo}) describes light reflection from

266 a sparse ensemble of surface objects casting shadows on the background assumed to be

267 Lambertian. The kernels are the only angle-dependent functions, the expressions of which are

268 given in Lucht et al. (2000). The band 3 BRDF coefficients spatially averaged over an actual

269 satellite FOV are used to calculate TOA radiance and GLER at 466 nm. To calculate GLER at 440

270 nm, we apply a scaling method using the ratio of OMI-derived lambert equivalent reflectivity

271 (LER) data at 440 nm and 466 nm:

272 $$GLER_{440} = GLER_{466} \times f_s. \tag{5}$$

273 The value of $f_s = \frac{LER_{440}}{LER_{466}}$ is taken from the gridded monthly LER ratio data at $1° \times 1°$ or coarser

274 resolution. The LER is determined from OMI TOA radiance measurements as discussed in

275 Vasilkov et al. (2017, 2018). We use clear-sky (effective cloud fraction <0.02) and aerosol free

276 (OMI UV Aerosol Index (Torres et al., 2007) <0.5) OMI LER data to create the monthly gridded

277 data. The cloud and aerosol screening is necessary because the spectral dependence of surface

278 features differ from that of clouds and aerosols.

279 Over water, the surface reflectance is calculated at the two wavelengths, 440 nm and 466 nm, using

280 VLIDORT. To calculate TOA radiance, we include light specularly reflected from a rough water

281 surface as well as diffuse light backscattered by water bulk. We also account for contributions

282 from oceanic foam that can be significant for high wind speeds. Reflection from the water surface

283   is described by the Cox–Munk slope distribution function, which depends on both the wind speed

284   and the wind direction (Cox and Munk, 1954). Polarization at the ocean surface is accounted for

285   by using a full Fresnel reflection matrix as suggested by Mishchenko and Travis (1997).

286   We use wind speed data from a pair of satellite microwave imagers that include the Advanced

287   Microwave Scanning Radiometer - Earth Observing System (AMSR-E) instrument onboard the

288   NASA Aqua satellite (Wentz and Meissner, 2004) for 2004-2011 and the Special Microwave

289   Imager/Sounder (SSMIS) onboard the Air Force Defense Meteorological Satellite Program

290   (DMSP) Satellite F16 (Wentz et al., 2012) afterwards. Wind direction data are taken from the

291   Global Modeling Assimilation Office (GMAO) Goddard Earth Observing System Model Forward

292   Processing for Instrument Teams (GEOS-5 FP-IT) near real time assimilation.

293   Diffuse light from the ocean is described by a Case 1 water model with a single input parameter

294   of chlorophyll concentration (Morel, 1988) taken from the monthly Aqua/MODIS data. The

295   common Case 1 water model developed for the Vis (Morel, 1988) was extended to the UV using

296   data from Vasilkov et al. (2002, 2005). To calculate water-leaving radiance, we require the

297   downwelling irradiance at the surface (i.e., atmospheric transmittance). Since the transmittance

298   and the water-leaving contribution are coupled, we develop a simple coupling scheme in

299   VLIDORT that ensures the value of water-leaving radiance used as an input at the ocean surface

300   will correspond to the correct value of the downwelling flux reaching the surface interface

301   (Fasnacht et al., 2019).

302   For OMI ground pixels covering land and water surfaces, the TOA radiance (I) is calculated as an

303   average of radiance for land (I_L) and water (I_w) weighted by the pixel land fraction (f):

304    $I = fI_L + (1 - f)I_w.$ (6)

305   The value of f is determined by converting various surface categories in the MODIS data (note

306   that these are of much higher spatial resolution than the OMI data) into a binary land-water mask

307   (e.g., treating all shorelines and ephemeral water as the land category and classifying all other

308   water sub-categories simply as water). The areal fraction of land (or water) for each OMI pixel is

309   then computed as the statistics of the binary categories.

310   Figure 2 shows an example of changes in surface reflectivity used in the previous (V3.1) and the

311   current (V4.0) version of the OMI NO_2 algorithm. The GLER data computed for OMI observations

312   as discussed above for March 20, 2005 differ considerably from the OMI-derived climatological

313   monthly LER data (Kleipool et al., 2008) for March. As shown in Figures 2 and 3(a), the GLERs

314   are generally lower than climatological LERs data except at swath edges with large viewing angles

315   and over areas affected by sunglint that correspond to higher values of GLER. Changes over the

316   sunglint areas are rather large, reaching up to 0.3. The climatological LER data derived by

317   analyzing histograms of five years of OMI-based LER data likely overestimate the actual surface

318   reflectivity due to residual cloud and aerosol contamination and underestimate over sunglint areas

319   as the procedure ignores sun glint affected observations. In contrast, the GLER data over land are

320   based on atmospherically corrected radiances from high-resolution MODIS observations,

321   minimizing the impact of both cloud and aerosols.

2.2.2 Improved cloud products retrieval

323   We develop a new algorithm that provides cloud parameters, namely cloud radiance fraction

324   (CRF) and cloud optical centroid pressure (OCP), and use them in the OMNO2 algorithm. Similar

325   to the standard OMCLDO2 algorithm (Veefkind et al, 2016), our cloud algorithm exploits the O_2-

326   O_2 absorption to retrieve O_2-O_2 SCD as discussed in Section 2.1.2, but derives the two cloud

327   parameters using the GLER and other ancillary data that are used in the NO_2 algorithm,

328   maintaining inter-algorithm consistency. The OMCLDO2 algorithm retrieves these parameters

329   using the climatological LER data from Kleipool et al. (2008). In the following, our new cloud

330   product is referred to as OMCDO2N.

331   The derivation of CRF and OCP is based on a simple cloud model called the mixed Lambertian-

332   equivalent reflectivity (MLER) model (Joiner and Vasilkov, 2006; Veefkind et al., 2016). The

333   MLER model treats cloud and ground as horizontally homogeneous, opaque Lambertian surfaces

334   and mixes them using the independent pixel approximation (IPA). According to the IPA, the

335   measured TOA radiance, I_m, is a sum of the clear-sky (I_g) and overcast (I_c) subpixel TOA

336   radiances that are weighted with an effective cloud fraction (ECF), f_c (e.g., Stammes et al., 2008):

337    $$I_m = I_g(1 - f_c) + I_c f_c. \qquad (7)$$

338   We choose the wavelength of 466 nm that is not substantially affected by rotational Raman

339   scattering (RRS) or atmospheric absorption to derive f_c. The parameters I_g and I_c are a function

340   of the ground and cloud LERs, respectively, and are calculated using VLIDORT (Spurr, 2006) and

341   obtained with an interpolated look up table. We use GLER discussed above for ground reflectivity

342 and a uniform cloud reflectivity of 0.8 (Koelemeijer et al., 2001; Stammes et al., 2008). The value
343 of f_c is calculated by inverting Equation (7). Note that aerosols are implicitly accounted for in the
344 determination of f_c, as they are treated (like clouds) as particulate scatters. CRF (f_r) defines the
345 fraction of TOA radiance reflected by cloud:

346 $$f_r = f_c \times \frac{I_c}{I_m}. \qquad (8)$$

347 We use pre-computed look-up tables of the TOA radiances generated using VLIDORT. Due to its
348 wavelength dependence, we calculate CRF at 466 nm for OCP at 440 nm for NO_2 retrievals.
349 The MLER model compensates for photon transport within a cloud by placing the Lambertian
350 surface somewhere in the middle of the cloud instead of at the top (Vasilkov et al., 2008). The
351 pressure of this surface corresponds to OCP, which can be modeled as a reflectance-averaged
352 pressure level reached by backscattered photons (Joiner et al., 2012). We retrieve cloud OCP from
353 the O_2-O_2 SCD discussed above (Section 2.1.2). The cloud OCP, P_c, is estimated by inversion
354 using the MLER method to compute the appropriate O_2-O_2 AMFs:

355 $$SCD = AMF_g \times VCD_g \times (1 - f_r) + AMF_c \times VCD_c \times f_r, \qquad (9)$$

356 where VCD (= SCD/AMF) is the vertical column density of O_2-O_2 over ground (VCD_g) and cloud
357 (VCD_c). The clear-sky (AMF_g) and overcast or cloudy (AMF_c) subpixel AMFs are calculated at
358 477 nm with ground (GLER) and cloud (0.8) reflectivity, respectively. Look-up tables for the
359 AMFs were generated using VLIDORT. Temperature profiles needed for estimation of VCD and
360 AMF are taken from the GEOS-5 global data assimilation system (Rienecker et al., 2011).

361 In addition to OCP, we retrieve the so-called scene pressure. The scene pressure is derived from
362 Eq. (9) assuming that $f_r = 1$ and cloud reflectivity = scene LER. The scene LER is determined
363 from the measured TOA radiance using the equation (Eq. 3) that defines TOA radiance in the
364 Rayleigh atmosphere over a Lambertian surface. In the absence of clouds, aerosols, and any major
365 gas absorptions, the scene pressure should be equal to the surface pressure. The scene pressure is
366 therefore an important diagnostic tool for evaluation of the performance of cloud pressure
367 algorithms.

368   Figure 4 shows an example of cloud products retrieved with our algorithm compared with those
369   retrieved from the standard OMCLDO2 algorithm (Veefkind et al., 2016). The retrieved OCP and
370   CRF from the two algorithms exhibit broadly consistent spatial patterns in both cloud altitude and
371   amount. The values of OCP generally range from 370 hPa to 1001 hPa in OMCDO2N versus 150
372   hPa to 1011 hPa in OMCLDO2N. For both products, CRF varies from 0 for clear-sky to 1 for
373   overcast conditions. A systematic difference is evident with generally higher values in OMCDO2N
374   for OCP by 147 hPa and CRF by 0.01 as compared to OMCLDO2. For OCP, there is a general
375   pattern in difference with OMCDO2N OCP higher for low-altitude clouds (>700 hPa) and lower
376   values for high-altitude clouds (<300 hPa) (Figure 3(c)). The largest OCP differences occur for
377   cases where cloud pressures in OMCLDO2 are clipped to 150 hPa. For CRF, larger differences
378   occur for partially cloudy scenes with higher CRF values in OMCDO2N by 0-0.1 for both land
379   and water surfaces (Figure 3(b)). Exceptions are over sun-glint areas, where CRF in OMCDO2N
380   is lower by 0-0.3 with the mean difference of 0.13.

381   **2.2.3 Treatment over snow and ice surfaces**

382   Over ice and snow surfaces, identified by the Near-real-time Ice and Snow Extent (NISE) flags
383   (Nolin et al., 2005) in the OMI Level 1b data, the following treatments are made for surface
384   reflectivity. In case of permanent ice and snow surfaces, the MCD43GF product provides BRDF
385   parameters, allowing us to calculate GLER. Over seasonal snow area usually with data gaps in
386   MCD43GF, we calculate OMI-derived LER but capped by a constant snow albedo of 0.6 following
387   Boersma et al. (2011). In rare cases of pixels not flagged by NISE and gaps in MODIS data, we
388   use OMI LER climatology (Kleipool et al., 2008), regardless whether the surface is either snow/ice
389   covered but missed by NISE or snow/ice free.

390   The OMI-derived scene reflectivity and scene pressure are used for NO_2 and cloud retrievals over
391   seasonal snow covered areas. If the NISE flags are set as true, the following assumptions are made
392   in our CRF, OCP, and NO_2 retrievals. Over bright surfaces (scene reflectivity > 0.2), we consider
393   the scenes as snow or cloud covered and assign the scene pressure to OCP. In addition, if a
394   difference between the surface pressure and scene pressure is smaller than 100 hPa, the scene is
395   considered to be either cloud free or covered by optically thin clouds following the cloud over
396   snow classification by Vasilkov et al. (2010), and CRF for the pixel is set to zero. If the difference
397   between the surface pressure and scene pressure exceeds 100 hPa, the scene is considered to be
398   overcast by optically thick (shielding) clouds (Vasilkov et al., 2010), and CRF for the pixel is set

399   to one. To avoid a possible NISE misclassification (Cooper et al., 2018) for low-reflectivity scenes

400   (scene reflectivity < 0.2), we consider such scenes as being snow/ice-free and calculate CRF, OCP,

401   and NO_2 AMF using the standard procedure with GLER for those scenes.

2.2.4 Improved terrain height/pressure calculation

403   Terrain pressure is a critical parameter to the AMF in NO_2 and cloud algorithms as well as to the

404   total optical depth of the Rayleigh atmosphere in the GLER algorithm. Prior studies have shown

405   that errors in terrain pressure can introduce over 20% errors in retrieved NO_2 VCD, especially in

406   areas of complex terrain (Zhou et al, 2010; Russell et al., 2011).

407   Here, we use a 2-arc minute Global Relief Model of global land-water surface data (ETOPOv2,

408   National Geophysical Data Center, 2006) to derive terrain height for each individual OMI ground

409   pixel. We derive the pixel-average terrain height by collocating and averaging the high resolution

410   data as discussed in Qin et al. (2019). The corresponding terrain pressure for each OMI pixel (P_s)

411   is calculated from the terrain pressure-height relationship established based on MERRA-2 monthly

412   terrain pressure (P_{s_GMI}) at a spatial resolution of 1° latitude × 1.25° longitude used in the GMI

413   model discussed above:

414    $$P_s = P_{s\_GMI} e^{-\left(\frac{\Delta z}{H}\right)},\tag{10}$$

415   where $\Delta z (= z - z_{GMI})$ represents the difference between the average terrain height for an OMI

416   pixel (z) and the terrain height at GMI resolution (z_{GMI}). The parameter, $H = \frac{kT}{Mg}$, represents the

417   scale height, where k is the Boltzmann constant, T is the temperature at the surface, M is the mean

418   molecular weight of air, and g is the acceleration due to gravity.

2.3 Impact of the changes on AMF

420   Figure 5 shows an example of how changes in each individual input parameter affect tropospheric

421   AMFs which, in turn, translate inversely to tropospheric NO_2 column retrievals. Replacing

422   climatological LER from OMLER with daily GLER data affects scattering weight profiles in the

423   lower troposphere, resulting in lower values of tropospheric AMF almost everywhere, except over

424   sun glint areas, where the use of GLER enhances scattering weights and tropospheric AMF (Figure

425   5(a)). The changes in tropospheric AMF with GLER usually range from -50% to 25%,

426   occasionally reaching up to -100%. The effect is small (-6% to 1%) for overcast scenes (CRF>0.9),

427 and increases (-28% to 17%) over clear and partially cloudy scenes (CRF<0.5), for unpolluted

428 regions, and surges (-62% to 3%) over polluted areas (>5×10^{15} molec. cm^{-2}). Figure 6(a) shows

429 GLER-driven changes in clear-sky (CRF<0.5) tropospheric AMF for different surface and scene

430 types, separated by tropospheric NO$_2$ column amounts. For 80% of cases over land, 97% over

431 water outside of sunglint areas, and 98% over sunglint areas, tropospheric NO$_2$ columns are <

432 1.5×10^{15} molec. cm^{-2} and the average GLER-driven differences are small at –6.6±17.3%, -

433 3.8±7.1%, and 4.0±12.9%, respectively. The differences increase gradually with column amount

434 over NO$_x$ source regions (e.g., cities and highly polluted coastal areas) with binned (of size 1×10^{15}

435 molec. cm^{-2}) average differences ranging from -10±20.1% to -30±19.7%. Over snow and ice

436 surfaces, changes are rather large, reaching up to a factor of two. The impact of change in the

437 surface reflection data on stratospheric AMFs is negligible (<2%).

438 Figures 5(b) and 6(b) show how changes in the cloud parameters (CRF and OCP) affect

439 tropospheric AMF. Replacing OMCLDO2-based cloud parameters with those from OMCDO2N

440 changes scattering weight profiles in a complicated way. Higher values of OCP in OMCDO2N

441 will include additional portions of scattering weights between the OMCDO2N- and OMCLDO2-

442 based OCPs, especially in the lower troposphere, thereby reducing the tropospheric AMF. On the

443 other hand, the higher CRF values lead to an increased contribution of the cloudy AMF in the

444 calculation of tropospheric AMF, thereby increasing its value. Their combination causes a wide

445 range of scenarios as well as large variation in the AMF effect. Overall, the change in cloud

446 parameters causes enhancement of tropospheric AMFs for partially cloudy and overcast scenes

447 and reduction for clear-sky scenes, especially over polluted areas. The AMF differences are

448 generally large for low AMF values that are driven by enhanced differences in either OCP, CRF,

449 or both as discussed in Vasilkov et al (2017). The changes in tropospheric AMF with the

450 OMCDO2N-based cloud parameters usually range from -17% to 28% with a larger variation over

451 land (-34% to 40%) as compared to water (-12% to 25%), and for low (<1) AMF (-47% to 41%)

452 as compared to high (>3) AMF (-4% to 18%). The largest changes in AMF (-96% to 62%) occur

453 over snow and ice surfaces that result from the difference in the treatment of snow and ice for

454 cloud and NO$_2$ retrievals as discussed in Section 2.2.3. For clear-sky and partially cloudy scenes

455 with CRF < 0.5, the effect of the changes in cloud parameters differs between land and water

456 surfaces as well as sunglint and non-sunglint geometries and becomes more pronounced over

457   polluted land and coastal areas (Figure 6b). As in the case of surface reflectivity, the impact of the

458   change in cloud parameters on stratospheric AMF is <1%.

459   Figure 5c presents an example of changes in tropospheric AMF differences between the previous

460   approach of using terrain pressure at OMI pixel centers and the pixel average terrain pressure

461   implemented in the current version (V4.0). In general, the AMF changes driven by the changes in

462   terrain pressure are within ±1% over ocean and ±3% over land, although at times they can reach

463   up to 30%, especially for observations over complex terrain such as mountainous regions (Figure

464   5c inset).

465   Figures 5d and 6c show the AMF differences arising from the combined effect of changes in all

466   parameters discussed above. The effect arising from the replacement of the climatological OMLER

467   with GLER is partially compensated by the effect arising from the change in cloud parameters in

468   places where the two parameters exhibit opposite trend. Exceptions are over polluted land and

469   coastal areas, the GLER effect on AMF is augmented by the cloud effect. The average AMF

470   changes arising from all parameters (2%) are lower than the changes arising from either GLER (-

471   2.3%) or cloud parameters (4.1%), although the combined effect leads to a wider range of variation

472   in AMF changes (-100% to 57%) as compared to the effect from individual parameters. The

473   changes arising from all parameters are somewhat smaller (-21% to 34%) for overcast scenes

474   (CRF>0.9) as compared to (-47% to 29%) over clear and partially cloudy scenes (CRF<0.5), and

475   are substantial (-137% to 30%) over highly polluted areas (>5×10^{15} molec. cm^{-2}) and over snow/ice

476   surfaces (-126% to 99%). Differences in the AMF effect are evident among land, water, and

477   sunglint areas (Figure 6c). The impact of the changes is below 1% for the stratospheric AMF.

478   **2.4 Row anomaly and removal of stripes**

479   The retrieved NO$_2$ SCDs have persistent relative biases in the 60 cross-track FOVs and show a

480   pattern of stripes running along each orbital track. This instrumental artifact is corrected using the

481   "de-striping" procedure described in detail in Bucsela et al (2013). Briefly, the de-striping

482   algorithm estimates the mean cross-track biases using measurements obtained at latitudes between

483   30S and 5N and from orbits within 2 orbits of target orbit. These correction values, one for each

484   cross-track position, are then subtracted from the retrieved SCDs to derive the de-striped SCD

485   field.

486   Starting June 25, 2007 and presumably even earlier, OMI experienced a more severe form of

487   anomaly that affects the quality of radiance data in certain rows at all wavelengths (Dobber et al.,

488   2008; Schenkeveld et al., 2017). This effect, called the "row anomaly" (RA), has developed and

489   changed over time. Currently, the RA has affected approximately half of the OMI's FOVs,

490   resulting in OMI's global coverage now in two days instead of one before the onset of the RA.

491   The quality of radiance data for the RA-affected FOVs is sufficiently poor as to prevent reliable

492   NO$_2$ retrievals. Therefore, we abandon retrieval calculations for all measurements that are flagged

493   by the RA-detection algorithm used in the Level-1 processing. We found that this RA-detection

494   algorithm may not be sufficiently sensitive to the relatively small (but important for our purposes)

495   RA changes. Figure 7 shows an example of anomalous rows not flagged by the RA-detection

496   algorithm but observed in the NO$_2$ retrievals. Shown are time series of average NO$_2$ SCDs

497   normalized by geometric AMFs over the Pacific Ocean for the RA-unaffected row of 20 (0-based)

498   compared with three rows that show significant degradation in the quality of SCD retrievals. These

499   particular rows are in the immediate proximity to the main RA area, thus showing the gradual RA

500   evolution: at the present epoch the RA slowly shifts towards the high-numbered rows – note the

501   sequential timing of the big drops in the retrievals in the rows 44-46. While the data from the three

502   rows start deviating from row 20 beginning from summer 2016, the data quality degrades further

503   for rows 44, 45, and 46 from September of 2017, 2018, and 2019, respectively, to the extent that

504   they cannot be sufficiently corrected by the de-striping algorithm. In such cases, we implement

505   additional RA-flagging for those rows that start showing anomalous behavior, and exclude those

506   data from Level-2 and higher level NO$_2$ products.

507   **2.5 Calculation of stratospheric and tropospheric NO$_2$ columns**

508   We use an observation-based stratosphere-troposphere separation scheme to estimate the

509   stratospheric NO$_2$ field as discussed in detail in Bucsela et al. (2013), and the algorithm remains

510   unchanged in the current version. Briefly, the stratospheric field for an orbit is computed by

511   creating a gridded global field of initial stratospheric NO$_2$ VCD estimates (V_{init}) with data

512   assembled from within ±7 orbits of the target orbit:

513            $$V_{init} = \frac{S_{strat}}{AMF_{strat}} = \frac{S - S_{trop\_ap}}{AMF_{strat}}. \tag{11}$$

514   Here S_{strat} and AMF_{strat} represent stratospheric SCD and AMF, respectively. An a priori

515   estimates of the tropospheric contribution (S_{trop_ap}) are subtracted from the measured, de-striped

516   SCDs (S), and grid cells where this contribution exceeds 0.3×10^{15} molecules cm^{-2} are masked.

517   This masking ensures that the model contribution to the retrieval is minimal, especially in the

518   polluted areas. The residual field of the initial stratospheric VCDs measured outside the masked

519   regions mainly over unpolluted or cloudy areas is smoothed by a boxcar average and a 2-

520   dimensional interpolation, yielding an estimate for stratospheric NO$_2$ VCD (V_{strat}) for an

521   individual ground pixel.

522   The estimation of the stratospheric NO$_2$ VCD allows for the computation of the tropospheric NO$_2$

523   VCD (V_{trop}) from the de-striped NO$_2$ SCD (S) and the tropospheric AMF (AMF_{trop}):

524             $$V_{trop} = \frac{S_{trop}}{AMF_{trop}} = \frac{S - S_{strat}}{AMF_{trop}}, \qquad\qquad (12)$$

525   where stratospheric NO$_2$ SCD (S_{strat}) is calculated from stratospheric AMF (AMF_{strat}) and V_{strat}

526   computed in the previous step.

527   With the updates in surface and cloud treatments as discussed in Section 2.2, the current version

528   has made significant improvements particularly in tropospheric AMFs and consequently in VCD

529   estimates. Further improvement to the retrievals is possible by enhancing the quality of a priori

530   NO$_2$ profiles through improvements in model resolution, emissions, and chemistry, which remain

531   unchanged in the current version. If improved a priori NO$_2$ profiles become available, one can first

532   use Eq. 1 to readily re-calculate AMF_{trop} by combining them with scattering weights ($w(z)$)

533   archived in the data files and then use Eq. 12 together with other supplied parameters to re-

534   calculate V_{trop}. The same approach can be applied to remove the effect of a priori profiles used in

535   retrievals altogether, while comparing NO$_2$ columns from a model simulation with retrievals

536   (Eskes and Boersma, 2003; Lamsal et al., 2014).

537   Figure 8 shows a comparison of tropospheric and stratospheric NO$_2$ columns retrieved from V3.1

538   and V4.0 algorithms for 20 March, 2005. As expected, the updates implemented in V4.0 yield

539   higher (~10–40%) tropospheric NO$_2$ columns in polluted areas, with less-pronounced (±10%)

540   differences in background and low-column areas. These results are consistent with the observed

541   differences in the tropospheric AMF as discussed above in Section 2.2.4 as well as with other

542   previous regional studies over land surfaces (Zhou et al, 2010; McLinden et al, 2014; Lin et al.,

543   2014, 2015; Laughner et al., 2019; Liu et al., 2019) that implemented one or more of the changes

544   applied in V4.0. In contrast to changes in tropospheric NO$_2$ retrievals, changes in stratospheric

545   NO$_2$ estimates range between -3.6$\times10^{14}$ molec. cm^{-2} and 3.2$\times10^{14}$ molec. cm^{-2} and are close to the

546   range of expected uncertainties of stratospheric NO_2 estimates (Bucsela et al., 2013). The relative

547   differences in stratospheric NO_2 column between the two versions is close to 0% on average,

548   usually range between -2.5% and 2.0%, and occasionally reach up to $\pm 13\%$. This difference in

549   stratospheric NO_2 estimates is much larger than the difference in stratospheric AMFs and is caused

550   by differences in tropospheric AMFs that influence NO_2 observations over unpolluted and cloudy

551   areas used by the stratosphere-troposphere separation scheme.

552   Figure 9 shows the seasonally averaged tropospheric NO_2 columns over the selected domains of

553   North America, Europe, southern Africa, and Asia for the months of June, July, and August in

554   2005. These domains contain highly polluted areas with significant NO_x emissions where the

555   impact of changes in surface reflectivity and cloud parameters on tropospheric NO_2 retrievals

556   becomes increasingly important. The use of more accurate pixel-specific information for surface

557   and cloud parameters in V4.0 results in significantly enhanced tropospheric NO_2 column retrievals

558   almost everywhere. The effect, however, varies with the vertical distribution of NO_2, with the

559   largest effects in high-column areas. This spatially-varying effect arising from algorithm changes

560   could have significant implications for estimates of trends and emissions of NO_x from satellite

561   observations.

562   Figure 10 shows the seasonal average tropospheric NO_2 columns for December through February.

563   While seasonal differences in NO_2 columns are evident owing to changes in NO_x lifetime and

564   boundary layer depth, the impact of algorithm changes in V4.0 remains similar. There are two

565   notable exceptions specifically related to observations over snow and ice surfaces. First, there are

566   significant data gaps in V3.1 but nearly none in V4.0. In V3.1, retrievals over snow and ice areas

567   were considered to be highly uncertain and therefore discarded, following the recommendation of

568   Boersma et al. (2011). As discussed above in Section 2.2.3, V4.0 incorporates changes in surface

569   and cloud treatment in NO_2 algorithm that allows us to retain more observations that we determine

570   to be our acceptable level of cloudiness. Next, these algorithm changes led to profound changes in

571   the calculated tropospheric AMFs and resulting NO_2 column amounts. The reduction in

572   tropospheric NO_2 retrievals in V4.0 over snow and ice covered surfaces arises from a combined

573   effect of enhanced values of surface reflectivity, their impact on the CRF and OCP retrievals, and

574   an inconsistent number of samples used in the calculation of the seasonal average. Nevertheless,

575   due to inferiority in the quality of BRDF data as well as complexities in separating snow from

576   clouds, caution is needed when interpreting winter time data at high latitudes.

577   Figure 11 shows some examples of how changes in the algorithm from V3.1 to V4.0 affect monthly

578   domain average tropospheric NO_2 columns over areas affected by various NO_x sources. In contrast

579   to minor changes over the pristine Pacific Ocean, month-to-month changes over source regions

580   vary considerably. The differences in tropospheric NO_2 columns between V4.0 and V3.1 range

581   from -11 to 15% over Beijing, China and from 0 to 29% over the Ruhr area in Germany, suggesting

582   variations in relative differences among cities and industrial areas. The changes over a major

583   biomass burning area of Democratic Republic of Congo, Angola, and Zambia range 13-56%

584   during the biomass burning season of May through August, but are <5% in other months.

585   Differences between the two versions are small over areas influenced by lightning NO_x emissions.

586

587   In Figure 12, we examine monthly variation of tropospheric NO_2 columns from the two versions

588   over five highly populated and polluted cities that vary in terrain types ranging from coastal (e.g.,

589   Shanghai, Tokyo) to mountainous (e.g., Mexico City). NO_2 columns in V4.0 are generally higher

590   than V3.1 by 0-30%, but the difference can occasionally reach up to 50% in some months. Changes

591   of that order of magnitude in highly polluted areas have implications for estimation of NO_x

592   emissions and trends using these data.

593   **3 Assessment of OMI NO_2 product**

594   In this section, we compare OMI NO_2 columns with total column retrievals from ground-based

595   Pandora measurements and integrated tropospheric columns from aircraft spirals at several

596   locations of the DISCOVER-AQ (Deriving Information on Surface Conditions from COlumn

597   and VERtically Resolved Observations Relevant to Air Quality) field campaign held between

598   2011 and 2014.

599   **3.1 Comparison between OMI and Pandora total column NO_2**

600   Here, we compare the total column NO_2 retrievals from OMI and the ground-based Pandora

601   spectrometer. Pandora is a compact sun-viewing remote sensing instrument that provides estimates

602   of NO_2 column amounts from the surface to the top of the atmosphere (Herman et al., 2009, 2018).

603   The NO_2 retrieval approach for Pandora is similar to that of OMI and consists of the DOAS spectral

604   fitting procedure to derive NO_2 SCD and its conversion to VCD using AMFs. However, the details

605   differ due to the lack of top-of-atmosphere radiance measurements for the spectral fitting and

606   simplicity in the AMF calculation for Pandora due to its direct sun measurements.

607   To compare with the OMI observations, we use Pandora data for sites listed in the Pandonia Global

608   Network (https://www.pandonia-global-network.org/). Out of 22 sites, we select 18 sites that we

609   determined to be suitable for comparison. Data from some of the sites (e.g., Rome, Italy) are

610   consistently higher than OMI by over a factor of two, suggesting that the sites may be in close

611   proximity to local sources that cannot be resolved by OMI. Although, some of the selected sites

612   have sporadic and short-term measurements (e.g., Ulsan, S. Korea), we consider them for

613   improved sampling and coverage. The collocation criteria include spatial and temporal matching

614   between OMI and Pandora observations by selecting the OMI pixels that encompass the Pandora

615   site and using Pandora 80-sec total NO_2 column data averaged over ±10 minutes of OMI

616   observations. We use high quality data obtained under clear sky conditions with root-mean-square

617   of spectral fitting residuals < 0.05 and NO_2 retrieval uncertainty < 0.05 DU (~1.3×10^{15} molec. cm$^-$

618   ^{2}) for Pandora and with CRF < 0.5 for OMI.

619   Figure 13 shows a comparison of OMI total NO_2 columns (sum of tropospheric and stratospheric

620   columns) with coincidently sampled Pandora direct-sun NO_2 column retrievals at a clean site of

621   Izaña in Tenerife Island, Spain, and a more polluted site in Greenbelt (Maryland, USA). The Izaña

622   Atmospheric Observatory is located on the top of a mountain plateau, with an elevation of 2373

623   meters above sea level. Since the site is free of local anthropogenic influences, Pandora

624   observations likely provide stratospheric and free tropospheric NO_2 amounts. In contrast, the

625   Greenbelt site in a suburban Washington DC area has traffic and air quality typical of polluted US

626   cities. As shown in Figures 13(a) and 13(b), OMI NO_2 retrievals from the two versions are highly

627   consistent (r>0.92) with somewhat higher values in V4.0 as compared to V3.1, by on average 13%

628   in Greenbelt and just 1% in Izaña. The variations of OMI NO_2 from both versions are also broadly

629   consistent with the Pandora measurements. The OMI and Pandora NO_2 columns are fairly

630   correlated (r = 0.32, N = 232) at Izaña, and moderately correlated (r = 0.51, N = 123) at Greenbelt;

631   often times the differences between each individual OMI and Pandora observations are significant.

632   Overall, the total column NO_2 data from OMI is higher than Pandora, with the average difference

633   of <16%. Occasional large discrepancies between OMI and Pandora reflect a combination of

634 spatial heterogeneity, differences in spatial and temporal sampling, differences in vertical
635 sensitivity of satellite and ground-based observations, and errors in OMI and Pandora retrievals.
636 Figures 13(c) and 13(d) show the multi-year monthly mean variation of OMI and Pandora NO_2
637 columns. The seasonal variation in Pandora and OMI NO_2 columns is highly consistent and
638 exhibits a summer maximum and a fall minimum at Izaña, and a winter maximum and summer
639 minimum in Greenbelt. The seasonal variation in the total column reflects that of the stratosphere
640 for Izaña and of the troposphere in Greenbelt. For Izaña, the monthly mean differences between
641 OMI and Pandora range from 8.2% in June to 38% in October for V4.0 and from 7.0% in June to
642 37% in October for V3.1. This discrepancy is likely due to the large aerial coverage of OMI pixels
643 including nearby cities, unlike the point measurements made by Pandora at the mountain top. The
644 average tropospheric NO_2 column observed by OMI is 8.9×10^{14} molec cm^{-2}, suggesting significant
645 NO_2 amounts in the troposphere with 20-32% contributions to total column NO_2 on a monthly
646 scale. For Greenbelt, the monthly mean differences between OMI and Pandora are within $\pm 12\%$
647 for the majority of the cases for both versions, with V4.0 improving agreement for February, April,
648 May and December, and worsening somewhat in other months, especially in September and
649 November, when the two versions exhibit larger differences in tropospheric NO_2 retrievals.
650 Figure 14 shows average total NO_2 columns measured by Pandora and OMI at the 18 selected
651 sites. Although there is a wide range of differences between individual sites, Pandora and OMI
652 observations exhibit a good spatial correlation, with slightly improved correlation for V4.0
653 (r=0.65, N=1082) as compared to V3.1 (r=0.62). The site-specific average values generally agree
654 to $\pm 35\%$ for columns $< 10^{16}$ molec. cm^{-2}. For more polluted sites, OMI retrievals tend to be lower
655 than the Pandora data. Although the relationship between Pandora and OMI has not changed
656 appreciably with the updates made in the OMI V4.0 product, the corrections are in the right
657 direction for a majority of the sites. The observed differences should not be interpreted as biases
658 in retrievals but rather as the combined effect of differences in spatial coverage, heterogeneity in
659 the NO_2 field, preferential placement of Pandora instruments, and potentially, a lack of site-
660 specific profile shapes assumed in OMI retrievals.

661 **3.2 Assessment using DISCOVER-AQ observations**

662 We also use NO_2 observations from the DISCOVER-AQ field program to assess OMI NO_2
663 retrievals. The DISCOVER-AQ campaign was composed of four field deployments: Baltimore-
664 Washington area in Maryland (MD) in July 2011; the San Joaquin Valley in California (CA) in

665   January-February 2013; Houston, Texas (TX) in September 2013; and Denver, Colorado (CO) in

666   July-August 2014. An observing strategy of the campaign was to carry out systematic and

667   concurrent in situ and remote sensing observations from a network of ground sites and research

668   aircraft that spiraled over each site 2-4 times a day. The payload of the P-3B research aircraft

669   included in situ measuring instruments to measure NO_2 profiles in the 0.3-5 km altitude range.

670   Each campaign hosted ground-based networks of surface monitors to provide in situ NO_2

671   observations as well as Pandora spectrometers to measure NO_2 column amounts.

672   We use Pandora NO_2 column observations and in situ NO_2 spiral data spatially and temporally

673   matched to OMI on clear and partially cloudy (cloud radiance fraction < 0.5) days. Airborne

674   measurements were carried out using the 4-channel chemiluminescence instrument from the

675   National Center for Atmospheric Research (Ridley and Grahek, 1990) and the Thermal

676   Dissociation Laser-Induced Florescence from the University of Berkeley (Thornton et al., 2000).

677   Despite differences in the measurement technique and sampling strategy, NO_2 measurements from

678   the two instruments are highly consistent and generally agree within 10%, with the exception of

679   ~32% difference for Houston (Choi et al., 2020). Here, we use the 1-second merged data from the

680   chemiluminescence instrument only, taking advantage of its high frequency measurements. The

681   spiral data are extended to the ground by using coincident in situ surface NO_2 measurements

682   sampled over the duration of spiral (~20 minutes). To account for NO_2 amounts in the missing

683   portion from the highest aircraft altitude to the tropopause, we use NO_2 from the GMI simulation.

684   Like the surface data, the Pandora total column NO_2 data are averaged over the duration of each

685   aircraft spiral. For OMI, we include data from all cross-track positions that are not subject to the

686   row anomaly.

687   Figure 15 and Table 2 show a summary of the comparison of OMI V4.0 and V3.1 NO_2 columns

688   with vertically integrated tropospheric columns from the P-3B aircraft at 20 spiral locations.

689   Overall, tropospheric NO_2 columns from OMI and aircraft spirals suggest a poor agreement but a

690   good correlation (r=0.74, N=100), with slightly improved agreement for V4.0 as compared to

691   V3.1. The agreement and correlations between OMI and P-3B observations vary by campaign

692   locations (e.g., r=0.4 for MD to r=0.81 for CA for V4.0). The level of improvements from V3.1 to

693   V4.0 also vary from 1.2% in TX to 9.8% in CA. OMI retrievals are usually lower than the aircraft

694   data, with larger differences for sites with larger NO_2 gradients and columns (e.g., Denver La Casa,

695   CO; Fresno, CA). OMI is rarely higher than the aircraft data as this usually happens over relatively

696   cleaner sites (e.g., Fairhill, MD). This alternating nature of the variation in results in polluted

697   versus clean areas suggests that OMI's large footprint size and narrow spiral radius (~4 km) of the

698   aircraft are likely the primary cause for the observed differences. This was demonstrated in Choi

699   et al. (2020) by using high-resolution Community Multi-scale Air Quality Model (CMAQ)

700   simulations. Additional contributions to the observed differences could come from OMI retrieval

701   errors arising from the use of a coarse resolution GMI-based a priori NO_2 profile shapes in the

702   AMF calculation. Such profile-related retrieval errors can be partially accounted for by replacing

703   GMI profiles with the aircraft observed NO_2 profiles (OMI_{obs}). The use of observed profiles in the

704   OMI retrievals from both versions leads to a slight change in correlation, but 20-35% reduction in

705   mean difference between OMI and aircraft observations, highlighting the role of a priori profiles

706   in NO_2 retrievals as suggested by previous studies (Russell et al., 2011; Lamsal et al., 2014;

707   Goldberg et al., 2017; Laughner et al., 2019; Choi et al., 2020). The campaign-average difference

708   between OMI and aircraft observations is -38.8% in V3.1 and -23.1% in V4.0, resulting in a net

709   improvement of 15.7% with V4.0. We note here that the aircraft observed profiles can be very

710   different from the actual profiles over OMI's FOVs (pixels) due to a difference in the sampling

711   domains for the two measurements.

712   Figure 15 and Table 3 also show the comparison between the OMI and Pandora total column

713   retrievals at the 20 DISCOVER-AQ sites. The correlations between collocated OMI V4.0 and

714   Pandora observations for individual campaign locations vary from fair (r=0.13 for MD) to good

715   (r=0.70 for CO), with a moderate correlation (r=0.56, N=83) for all observations from the four

716   locations. The changes in correlation from V3.1 to V4.0 are generally small with a minor

717   improvement in CA and deterioration in MD. As compared to the aircraft observations, the OMI

718   data generally show better agreement with the Pandora retrievals, with the smallest difference in

719   MD and the largest difference in CO. As compared to V3.1, the agreement is improved for V4.0

720   by up to 9%. The use of aircraft-observed NO_2 profiles in AMF calculations leads to higher OMI

721   column retrievals than those from Pandora for MD and TX, and lower columns than Pandora for

722   CA and CO. Overall, total column retrievals from OMI V3.1 and V4.0 are respectively 33.5% and

723   16.3% lower than Pandora; this change is consistent with the comparison between OMI and P-3B

724   observations. The observed discrepancy between the OMI, aircraft spiral, and Pandora data points

725 to general difficulties in comparing observations of different spatial resolutions for a short-lived

726 trace gas like NO_2 that has large spatial gradients, especially in the boundary layer.

4 Conclusions

728 We have described a series of significant improvements made to the operational OMI NO_2

729 Standard Product (OMNO2) algorithm. The new version, version 4.0 (V4.0), of the OMNO2

730 product, released recently to the public at the NASA Goddard Earth Sciences Data and Information

731 Services Center (GES DISC), mainly relies on improved methods and high-resolution inputs for a

732 more accurate determination of air mass factors (AMFs). Major improvements include (1) a new

733 O_2-O_2 cloud algorithm to estimate cloud radiance fraction (CRF) and cloud optical centroid

734 pressure (OCP), both required for the AMF calculation; 2) a new MODIS BRDF-derived

735 geometry-dependent surface Lambertian Equivalent Reflectivity (GLER) input data used in both

736 the NO_2 and cloud retrievals; (3) improved terrain pressure calculated for OMI's footprint; and (4)

737 improved surface and cloud treatments over snow and ice surfaces. Over open-water areas, inputs

738 to the GLER calculations include chlorophyll concentrations from MODIS, the wind speed data

739 from the Advanced Microwave Scanning Radiometer–Earth Observing System (AMSR-E) and

740 the Special Microwave Imager–Sounder (SSMIS) instruments, and the wind direction data from

741 the NASA GEOS-5 model. The following algorithmic steps remain unchanged: the scheme for

742 separating stratospheric and tropospheric components, first implemented in Version 2.1 (Bucsela

743 et al., 2013; Lamsal et al., 2014); an optimized spectral fitting algorithm used for NO_2 slant column

744 density retrievals (Marchenko et al., 2015); and the use of annually varying monthly mean Global

745 Modeling Initiative (GMI) derived inputs (e.g., NO_2 vertical profile shapes), as implemented in

746 Version 3.0 (Krotkov et al., 2017).

747 The changes in inputs result in substantial changes tropospheric AMFs (and thus VCDs) in V4.0

748 relative to the previous version (V3.1). The geometry-dependent GLER data computed for OMI

749 observations used in V4.0 differ considerably from the OMI-derived climatological LER data

750 (Kleipool et al., 2008) used in V3.1. The data from GLER (a unitless value with 0.0-1.0 range) are

751 generally lower, by <0.05, than the climatological LER data over land and ocean outside of

752 sunglint areas; GLER is much higher over the sunglint areas that reaches more than 0.3 due to the

753 geometry-dependent Fresnel reflection. The cloud parameters (OCP and CRF) retrieved from the

754 new O_2-O_2 cloud algorithm described here and those from the operational cloud algorithm

755 (Veefkind et al., 2016) used in V3.1 exhibit significant differences with generally larger values for
756 both parameters in V4.0 as compared to V3.1, with noticeable exceptions over sunglint areas,
757 where CRFs in V4.0 are lower than V3.1 by <0.3. Over snow and ice surfaces, identified by the
758 Near-real-time Ice and Snow Extent (NISE) flags in the OMI L1b data, various adjustments are
759 made in V4.0 for GLER, OCP, and CRF by using other diagnostic parameters (e.g., scene pressure)
760 retrieved by the new cloud algorithm. The scattering weights and tropospheric AMFs for NO_2
761 respond to the changes in these input parameters in a complicated way. Typically, tropospheric
762 AMFs decrease with the use of GLER and increase with the use of the new cloud parameters, with
763 exceptions over water surfaces affected by sunglint, where we observe the opposite effect. Over
764 highly polluted areas, the effect from GLER is augmented by the effect from the new cloud
765 parameters, resulting in a considerable decrease in the tropospheric AMF. Changes in tropospheric
766 AMFs resulting from the updates in treatment of the snow and ice-covered areas are also
767 significant. Changes in the adopted terrain pressure (V4.0 vs V3.1) can also have a sizable effect
768 on tropospheric AMFs, particularly over areas with a complex terrain. In contrast, for stratospheric
769 AMFs the combined impact of all of these algorithmic updates is negligible.

770 The changes in tropospheric AMFs translate directly into changes in tropospheric NO_2 retrievals
771 and indirectly into stratospheric NO_2 estimates. Over background and low column NO_2 areas,
772 tropospheric NO_2 column estimates have not changed appreciably from V3.1 to V4.0. Over more
773 polluted areas, the tropospheric NO_2 retrievals have typically increased by 10-40% from V3.1 to
774 V4.0, mostly in a direct proportion to the pollution level. Most of the increase in the highly polluted
775 areas is driven by the change in the surface reflectivity data used in the AMF calculation, with
776 additional increase due to changes in the cloud parameters. Changes in the stratospheric NO_2
777 estimates are usually within ±2.5%, which is close to the range of estimated uncertainties of
778 stratospheric NO_2 estimates.

779 A global assessment of V4.0 tropospheric and stratospheric NO_2 products was performed by a
780 thorough evaluation of their consistency with the data from V3.1, which was carefully evaluated
781 in our previous works (e.g., Krotkov et al., 2017; Choi et al., 2020). In addition, we use
782 NO_2 measurements made by independent ground- and aircraft-based instruments to evaluate the
783 V4.0 product. The comparison of OMI total column NO_2 data with collocated Pandora
784 observations at its 18 global network and 20 DISCOVER-AQ locations suggests that OMI and
785 Pandora are generally highly consistent, exhibit similar seasonal variation, and agree within their

786   expected uncertainties of 2.7×10^{15} molec cm^{-2} for Pandora (Herman et al., 2009) and ~30% for
787   OMI under clear-sky conditions (Boersma et al., 2011; Bucsela et al., 2013). Individual data points
788   differ considerably, and OMI tends to be lower than Pandora over highly polluted areas with
789   spatially inhomogeneous NO$_2$. The comparison of OMI tropospheric NO$_2$ column retrievals with
790   columns derived from the aircraft spirals and surface data during the DISCOVER-AQ campaign
791   also suggests general agreement in spatial variation, but OMI values are about a factor of two
792   lower in polluted environments. This difference is due partly to inaccurate a priori assumptions,
793   but primarily to OMI's relatively large pixels. The use of observed NO$_2$ profiles as a priori
794   information reduces the bias from ~50% to 23%, on average. The Multiple-Axis Differential
795   Optical Absorption Spectrometer (MAX-DOAS) (e.g., Chan et al., 2019) or high spatial resolution
796   measurements from aircraft (e.g., Nowlan et al., 2016; Lamsal et al., 2017; Judd et al., 2019) would
797   provide a more comprehensive validation by mapping the NO$_2$ distributions over the complete
798   areas of aircraft spirals and the satellite FOVs.

799   In this study, we focused on improving the surface and cloud parameters in the NASA standard
800   NO$_2$ product retrievals. To further improve the retrieval accuracy, it is important to incorporate
801   improved retrieval methods and auxiliary information, such as high resolution a priori NO$_2$
802   profiles. For instance, current cloud algorithms based on the MLER model treat aerosols implicitly
803   by providing effective (cloud + aerosol) CRF and effective cloud OCP, both necessary inputs for
804   AMF calculations. Cloud effects on trace gas retrievals can be compromised by the unknown
805   aerosol effects, which lead to errors in AMF calculations. Therefore, the use of the GLER product
806   in the NO$_2$ algorithm will greatly benefit from an explicit accounting for aerosol effects,
807   particularly over polluted regions. We have recently developed an explicit and consistent aerosol
808   correction method which can be applied consistently in both the cloud and NO$_2$ retrievals
809   (Vasilkov et al. 2020); it uses a model of the aerosol optical properties from a global aerosol
810   assimilation system paired with radiative transfer calculations. This approach allows us to account
811   for aerosols within the OMI cloud and NO$_2$ algorithms with relatively small changes and will be
812   used in the next version of the NO$_2$ algorithm.

813

814   **Code/Data availability:** The Level-2 swath type column NO$_2$ products (OMNO2) is available
815   from the NASA Goddard Earth Sciences Data and Information Services Center (GES DISC)
816   website (https://disc.gsfc.nasa.gov/datasets/OMNO2G_003/summary). Other OMNO2-associated

817   NO_2 products such as the Level-2 gridded column product, OMNO2G, and the Level-3 gridded

818   column product, OMNO2d, both sampled at regular 0.25° latitude x 0.25° longitude wide grids are

819   distributed through the NASA GES-DISC

820   (https://disc.gsfc.nasa.gov/datasets/OMNO2d_003/summary) and GIOVANNI

821   (https://giovanni.gsfc.nasa.gov/giovanni/) websites. An additional high spatial resolution (0.1° x

822   0.1° latitude-longitude grid) OMNO2d product (OMNO2d_HR) is also made available through

823   the NASA AVDC website

824   (https://avdc.gsfc.nasa.gov/pub/data/satellite/Aura/OMI/V03/L3/OMNO2d_HR/). The AVDC

825   website also hosts overpass files for several hundred sites around the globe

826   (https://avdc.gsfc.nasa.gov/pub/data/satellite/Aura/OMI/V03/L2OVP/OMNO2/).

827

828   *Author contributions.* LNL, NAK, JJ, and AV designed the data analysis. WQ, ZF, NAK, DH,

829   and AV developed and evaluated the GLER product. EY, SM, AV, NAK, JJ, and BF developed

830   and evaluated the cloud product. LNL, NAK, SM, WHS, and EB have developed and evaluated

831   the NASA NO_2 Standard Product. LNL and SC conducted validation of the OMI NO_2 products

832   using Pandora and other independent observations. LNL, AV, SM, and ZF wrote the manuscript

833   with comments from all coauthors.

834

835   *Competing interests.* The authors declare no competing interests.

836

837   *Acknowledgements.* We acknowledge the NASA Earth Science Division for funding OMI NO_2

838   product development and analysis. The Dutch–Finnish-built OMI instrument is part of the NASA

839   EOS Aura satellite payload. KNMI and the Netherlands Space Agency (NSO) manage the OMI

840   project. We acknowledge the NASA Pandora, ESA-Pandonia, and NASA's DISCOVER-AQ

841   projects for free access to the data. We thank the two anonymous reviewers for their helpful

842   comments.

843

References

Beirle, S., Boersma, K. F., Platt, U., Lawrence, M. G., and Wagner, T.: Megacity emissions and lifetimes of nitrogen oxides probed from space, *Science*, *333*, 1737–1739. https://doi.org/10.1126/science.1207824, 2011.

Berezin, E. V, Konovalov, I. B., Ciais, P., Richter, A., Tao, S., Janssens-Maenhout, G., et al.: Multiannual changes of CO_2 emissions in China: indirect estimates derived from satellite measurements of tropospheric NO_2 columns, *Atmos. Chem. Phys*, *13*, 9415–9438. https://doi.org/10.5194/acp-13-9415-2013, 2013.

Boersma, K. F., Eskes, H. J., Dirksen, R. J., van der A, R. J., Veefkind, J. P., Stammes, P., Huijnen, V., Kleipool, Q. L., Sneep, M., Claas, J., Leitão, J., Richter, A., Zhou, Y., and Brunner, D.: An improved tropospheric NO_2 column retrieval algorithm for the Ozone Monitoring Instrument, *Atmos. Meas. Tech.*, 4, 1905–1928, https://doi.org/10.5194/amt-4-1905-2011, 2011.

Boersma, K. F., Eskes, H. J., Richter, A., De Smedt, I., Lorente, A., Beirle, S., van Geffen, J. H. G. M., Zara, M., Peters, E., Van Roozendael, M., Wagner, T., Maasakkers, J. D., van der A, R. J., Nightingale, J., De Rudder, A., Irie, H., Pinardi, G., Lambert, J.-C., and Compernolle, S. C.: Improving algorithms and uncertainty estimates for satellite NO_2 retrievals: results from the quality assurance for the essential climate variables (QA4ECV) project, *Atmos. Meas. Tech.*, 11, 6651–6678, https://doi.org/10.5194/amt-11-6651-2018, 2018.

Bucsela, E.J., Celarier, E.A., Wenig, M.O., Gleason, J.F., Veefkind, J.P., Boersma, K.F., and Brinksma, E.J.: Algorithm for NO_2 vertical column retrieval from the Ozone Monitoring Instrument, *IEEE Trans. Geosci. Remote Sens.*, 44, 5, 2006.

Bucsela, E. J., Krotkov, N. A., Celarier, E. A., Lamsal, L. N., Swartz, W. H., Bhartia, P. K., Boersma, K. F., Veefkind, J. P., Gleason, J. F., and Pickering, K. E.: A new stratospheric and tropospheric NO_2 retrieval algorithm for nadir-viewing satellite instruments: applications to OMI, *Atmos. Meas. Tech.*, 6, 2607–2626, https://doi.org/10.5194/amt-6-2607-2013, 2013.

Cai, K., Li, S., Zheng, F., Yu, C., Zhang, X., Liu, Y., and Li, Y.: Spatio-temporal Variations in NO_2 and $PM_{2.5}$ over the Central Plains Economic Region of China during 2005-2015 Based on Satellite Observations, *Aer. Air Qual. Res.*, 5, 1221–1235, 10.4209/aaqr.2017.10.0394, 2018.

Canty, T. P., Hembeck, L., Vinciguerra, T. P., Anderson, D. C., Goldberg, D. L., Carpenter, S.

F., Allen, D. J., Loughner, C. P., Salawitch, R. J., and Dickerson, R. R.: Ozone and NO_x chemistry in the eastern US: evaluation of CMAQ/CB05 with satellite (OMI) data, *Atmos. Chem. Phys.*, 19, 10965–10982, 10.5194/acp-15-10965-2015, 2015.

Castellanos, P., and Boersma, K. F.: Reductions in nitrogen oxides over Europe driven by environmental policy and economic recession, *Sci. Rep.*, 1, 10.1038/srep00265, 2012.

Celarier, E. A., et al: Validation of Ozone Monitoring Instrument nitrogen dioxide columns, *J. Geophys. Res.*, 113, D15S15, doi:10.1029/2007JD008908, 2008.

Chance, K., Kurosu, T.P., and Sioris, K.E.: Undersampling correction for array detector-based satellite spectrometers, *Appl. Opt.*, 44, 1296– 1304, 2005.

Chan, K. L., Wang, Z., Ding, A., Heue, K.-P., Shen, Y., Wang, J., Zhang, F., Shi, Y., Hao, N., and Wenig, M.: MAX-DOAS measurements of tropospheric NO_2 and HCHO in Nanjing and a comparison to ozone monitoring instrument observations, *Atmos. Chem. Phys.*, 19, 10051– 10071, https://doi.org/10.5194/acp-19-10051-2019, 2019.

Choi, S., Lamsal, L. N., Follette-Cook, M., Joiner, J., Krotkov, N. A., Swartz, W. H., Pickering, K. E., Loughner, C. P., Appel, W., Pfister, G., Saide, P. E., Cohen, R. C., Weinheimer, A. J., and Herman, J. R.: Assessment of NO_2 observations during DISCOVER-AQ and KORUS-AQ field campaigns, Atmos. Meas. Tech., 13, 2523–2546, https://doi.org/10.5194/amt-13-2523-2020, 2020.

Cooper, M.J., Martin, R.V., Lyapustin, A.I., and McLinden, C.A.: Assessing snow extent data sets over North America to inform and improve trace gas retrievals from solar backscatter, *Atmos. Meas. Tech.*, 11, 2983-2994, https://doi.org/10.5194/amt-11-2983-2018, 2018.

Cox, C. and Munk, W.: Statistics of the sea surface derived from sun glitter, *J. Mar. Res.*, 13, 198– 227, 1954.

de Foy, B., Lu, Z., Streets, D. G., Lamsal, L. N., and Duncan, B. N.: Estimates of power plant NO_x emissions and lifetimes from OMI NO_2 satellite retrievals. *Atmos. Environ.*, *116*, 1–11, https://doi.org/10.1016/j.atmosenv.2015.05.056, 2015.

Dirksen, R., Dobber, M., Voors, R, and Levelt, P.: Prelaunch characterization of the Ozone Monitoring Instrument transfer function in the spectral domain, *Appl. Opt.*, 45, 3972– 3981, 2006.

Dix, B., Bruin, J., Roosenbrand, E., Vlemmix, T., Francoeur, C., Gorchov-Negron, A., McDonald, B., Zhizhin, M., Elvidge, C., Veefkind, P., Levelt, P., and de Gouw,

906   J.: Nitrogen Oxide Emissions from U.S. Oil and Gas Production: Recent Trends and Source
907   Attribution, *Geophys. Res. Lett.*, 1, e2019GL085866, 10.1029/2019gl085866, 2020.

908   Dobber, M., Kleipool, Q., Dirksen, R., Levelt, P. F., Jaross, G., Taylor, S., et al.: Validation of
909   Ozone Monitoring Instrument level 1b data products. *J. Geophys. Res.*,
910   https://doi.org/10.1029/2007JD008665, 2008.

911   Douglass, A. R., Stolarski, R.S., Strahan, S.E., and Connell, P.S.: Radicals and reservoirs in the
912   GMI chemistry and transport model: Comparison to measurements, *J. Geophys. Res.*, 109,
913   D16302, doi:10.1029/2004JD004632, 2004.

914   Duncan, B. N., Yoshida, Y., Foy, B., Lamsal, L. N., Streets, D. G., Lu, Z., Pickering, K. E., and
915   Krotkov, N. A.: The observed response of Ozone Monitoring Instrument (OMI) NO$_2$ columns
916   to NOx emission controls on power plants in the United States: 2005–2011, *Atmos. Environ.*,
917   102–111, 10.1016/j.atmosenv.2013.08.068, 2013.

918   Duncan, B.N., Lamsal, L.N., Thompson, A.M., Yoshida, Y., Lu, Z., Streets, D.G., Hurwitz, M.M.,
919   Pickering, K.E.: A space-based, high-resolution view of notable changes in urban NO$_x$
920   pollution around the world (2005-2014), *J. Geophys. Res.*, 121, 976–996,
921   doi:10.1002/2015JD024121, 2016.

922   Eskes, H. J. and Boersma, K. F.: Averaging kernels for DOAS total-column satellite retrievals,
923   *Atmos. Chem. Phys.*, 3, 1285–1291, https://doi.org/10.5194/acp-3-1285-2003, 2003.

924   Fasnacht, Z., Vasilkov, A., Haffner, D., Qin, W., Joiner, J., Krotkov, N., Sayer, A. M., and Spurr,
925   R.: A geometry-dependent surface Lambertian-equivalent reflectivity product for UV–Vis
926   retrievals – Part 2: Evaluation over open ocean, *Atmos. Meas. Tech.*, 12, 6749–6769,
927   https://doi.org/10.5194/amt-12-6749-2019, 2019.

928   Geddes, J. A. and Martin, R. V.: Global deposition of total reactive nitrogen oxides from 1996 to
929   2014 constrained with satellite observations of NO$_2$ columns, *Atmos. Chem. Phys.*, 17,
930   10071–10091, https://doi.org/10.5194/acp-17-10071-2017, 2017.

931   Gelaro, R., McCarty, W., Suárez, M.J., Todling, R., Molod, A., Takacs, L., Randles, C.A.,
932   Darmenov, A., Bosilovich, M.G., Reichle, R., Wargan, K., Coy, L., Cullather, R., Draper, C.,
933   Akella, S., Buchard, V., Conaty, A., da Silva, A.M., Gu, W., Kim, G., Koster, R., Lucchesi,
934   R., Merkova, D., Nielsen, J.E., Partyka, G., Pawson, S., Putman, W., Rienecker, M., Schubert,
935   S.D., Sienkiewicz, M., and Zhao, B.: The Modern-Era Retrospective Analysis for Research
936   and Applications, Version 2 (MERRA-2). *J. Climate,* 30, 5419–

5454, https://doi.org/10.1175/JCLI-D-16-0758.1, 2017.

Ghude, S. D., Kulkarni, S. H., Jena, C., Pfister, G. G., Beig, G., Fadnavis, S., and A, R. J.: Application of satellite observations for identifying regions of dominant sources of nitrogen oxides over the Indian Subcontinent, *J. Geophys. Res.*, 2, 1075–1089, 10.1029/2012jd017811, 2013.

Goldberg, D. L., Lamsal, L. N., Loughner, C. P., Swartz, W. H., Lu, Z., and Streets, D. G.: A high-resolution and observationally constrained OMI NO_2 satellite retrieval. *Atmos. Chem. Phys.*, *17*, 11403–11421. https://doi.org/10.5194/acp-17-11403-2017, 2017.

Goldberg, D. L., Saide, P. E., Lamsal, L. N., de Foy, B., Lu, Z., Woo, J.-H., et al.: A top-down assessment using OMI NO_2 suggests an underestimate in the NO_x emissions inventory in Seoul, South Korea, during KORUS-AQ. *Atmos. Chem. Phys.*, *19*, 1801–1818. https://doi.org/10.5194/acp-19-1801-2019, 2019a.

Goldberg, D., Lu, Z., Oda, T., Lamsal, L.N, Liu, F., Griffin, D., McLinden, C., Krotkov, N.A., Duncan, B.N., Streets, D.: Exploiting OMI NO_2 satellite observations to infer fossil-fuel CO_2 emissions from U.S. megacities, *Sci. Tot. Environ.*, 695, 133805, 10.1016/j.scitotenv.2019.133805, 2019b.

Gu, J., Chen, L., Yu, C., Li, S., Tao, J., Fan, M., Xiong, X., Wang, Z., Shang, H., and Su, L.: Ground-Level NO_2 Concentrations over China Inferred from the Satellite OMI and CMAQ Model Simulations, *Rem. Sens.*, 6, 519, 10.3390/rs9060519, 2017.

Han, K., Lee, C., Lee, J., Kim, J., and Song, C.: A comparison study between model-predicted and OMI-retrieved tropospheric NO_2 columns over the Korean peninsula, *Atmos. Environ.*, 17, 2962–2971, 10.1016/j.atmosenv.2010.10.016, 2011.

Herman, J., Cede, A., Spinei, E., Mount, G., Tzortziou, M., and Abuhassan, N.: NO_2 column amounts from ground-based Pandora and MFDOAS spectrometers using the direct-sun DOAS technique: Intercomparisons and application to OMI validation, *J. Geophys. Res. Atmos.*, 114, D13, https://doi.org/10.1029/2009JD011848, https://agupubs.onlinelibrary.wiley.com/doi/abs/10.1029/2009JD011848, 2009.

Herman, J., Spinei, E., Fried, A., Kim, J., Kim, J., Kim, W., Cede, A., Abuhassan, N., and Segal-Rozenhaimer, M.: NO_2 and HCHO measurements in Korea from 2012 to 2016 from Pandora spectrometer instruments compared with OMI retrievals and with aircraft measurements during the KORUS-AQ campaign, *Atmos. Meas. Tech.*, 11, 4583–4603,

https://doi.org/10.5194/amt-11-4583-2018, https: //www.atmos-meas-tech.net/11/4583/2018/, 2018.

Herron-Thorpe, F. L., Lamb, B. K., Mount, G. H., and Vaughan, J. K.: Evaluation of a regional air quality forecast model for tropospheric NO_2 columns using the OMI/Aura satellite tropospheric NO_2 product, *Atmos. Chem. Phys.*, 18, 8839–8854, 10.5194/acp-10-8839-2010, 2010.

Hudman, R. C., Moore, N. E., Mebust, A. K., Martin, R. V., Russell, A. R., Valin, L. C., and Cohen, R. C.: Steps towards a mechanistic model of global soil nitric oxide emissions: implementation and space based-constraints, *Atmos. Chem. Phys.*, 16, 7779–7795, 10.5194/acp-12-7779-2012, 2012.

Ialongo, I., Herman, J., Krotkov, N., Lamsal, L., Boersma, K. F., Hovila, J., and Tamminen, J.: Comparison of OMI NO_2 observations and their seasonal and weekly cycles with ground-based measurements in Helsinki, *Atmos. Meas. Tech.*, 10, 5203–5212, 10.5194/amt-9-5203-2016, 2016.

Joiner, J., Bhartia, P., Cebula, R., Hilsenrath, E., McPeters, R., and Park, H.: Rotational Raman scattering (Ring effect) in satellite backscatter ultraviolet measurements, *Appl. Opt.*, 34, 4513-4525, 1995.

Joiner J. and Vasilkov, A. P.: First Results from the OMI Rotational-Raman Scattering Cloud Pressure Algorithm, *IEEE Trans. Geophys. Remote Sens.*, 44, 1272–1282, 2006.

Joiner, J., Vasilkov, A. P., Gupta, P., Bhartia, P. K., Veefkind, P., Sneep, M., de Haan, J., Polonsky, I., and Spurr, R.: Fast simulators for satellite cloud optical centroid pressure retrievals; evaluation of OMI cloud retrievals, *Atmos. Meas. Tech.*, 5, 529–545, https://doi.org/10.5194/amt-5-529-2012, 2012.

Judd, L. M., Al-Saadi, J. A., Janz, S. J., Kowalewski, M. G., Pierce, R. B., Szykman, J. J., Valin, L. C., Swap, R., Cede, A., Mueller, M., Tiefengraber, M., Abuhassan, N., and Williams, D.: Evaluating the impact of spatial resolution on tropospheric NO_2 column comparisons within urban areas using high-resolution airborne data, *Atmos. Meas. Tech.*, 12, 6091–6111, https://doi.org/10.5194/amt-12-6091-2019, 2019.

Kim, H. C., Lee, P., Judd, L., Pan, L., and Lefer, B.: OMI NO_2 column densities over North American urban cities: the effect of satellite footprint resolution, *Geos. Mod. Develop.*, 3, 1111–1123, 10.5194/gmd-9-1111-2016, 2016.

999   Kleipool, Q. L., Dobber, M. R., de Haan, J. F., and Levelt, P. F.: Earth surface reflectance
1000   climatology from 3 years of OMI data, *J. Geophys. Res.*, 113, D18308,
1001   doi:10.1029/2008JD010290, 2008.

1002   Koelemeijer, R. B. A., Stammes, P., Hovenier, J. W., and de Haan, J. F.: A fast method for
1003   retrieval of cloud parameters using oxygen A-band measurements from the Global Ozone
1004   Monitoring Experiment, *J. Geophys. Res.,* 106, 3475–3496, 2001.

1005   Konovalov, I. B., Berezin, E. V., Ciais, P., Broquet, G., Zhuravlev, R. V., and Janssens-Maenhout,
1006   G.: Estimation of fossil-fuel CO_2 emissions using satellite measurements of "proxy" species.
1007   *Atmos. Chem. Phys.*, *16*(21), 13509–13540. https://doi.org/10.5194/acp-16-13509-2016,
1008   2016.

1009   Krotkov, N. A., McLinden, C. A., Li, C., Lamsal, L. N., Celarier, E. A., Marchenko, S.
1010   V., Swartz, W. H., Bucsela, E. J., Joiner, J., Duncan, B. N., Boersma, K..F., Pepijn, J.P.,
1011   Levelt, P.F., Fioletov, V.E., Dickerson, R. R., He, H., Lu, Z., and D. G. Streets, D.G.: Aura
1012   OMI observations of regional SO_2 and NO_2 pollution changes from 2005 to 2015, *Atmos.*
1013   *Chem. Phys.*, 7, 4605–4629, 10.5194/acp-16-4605-2016, 2016.

1014   Krotkov, N. A., Lamsal, L. N., Celarier, E. A., Swartz, W. H., Marchenko, S. V., Bucsela, E. J., et
1015   al.: The version 3 OMI NO_2 standard product. *Atmos. Meas. Tech.*, *10*, 3133–3149.
1016   https://doi.org/10.5194/amt-10-3133-2017, 2017.

1017   Kuhlmann, G., Lam, Y. F., Cheung, H. M., Hartl, A., Fung, J. C. H., Chan, P. W., and Wenig, M.
1018   O.: Development of a custom OMI NO_2 data product for evaluating biases in a regional
1019   chemistry transport model, *Atmos. Chem. Phys.*, 15, 5627–5644, https://doi.org/10.5194/acp-
1020   15-5627-2015, 2015.

1021   Lamsal, L.N., Martin, R.V., van Donkelaar, A., Celarier, E.A., Bucsela, E.J., Boersma, K.F.,
1022   Dirksen, R., Luo, C., and Wang, Y.: Indirect validation of tropospheric nitrogen dioxide
1023   retrieved from the OMI satellite instrument: Insight into the seasonal variation of nitrogen
1024   oxides at northern midlatitude, *J. Geophys. Res.*, 115, doi:10.1029/2009JD013351, 2010.

1025   Lamsal, L.N., Martin, R.V., Parrish D.D., and Krotkov, N.A.: Scaling relationship for NO_2
1026   pollution and population size: A satellite perspective, *Environ. Sci. Technol*, 47, 7855-7861,
1027   2013.

1028   Lamsal, L. N., Krotkov, N. A., Celarier, E. A., Swartz, W. H., Pickering, K. E., Bucsela, E. J.,
1029   Gleason, J. F., Martin, R. V., Philip, S., Irie, H., Cede, A., Herman, J., Weinheimer, A.,

Szykman, J. J., and Knepp, T. N.: Evaluation of OMI operational standard NO_2 column retrievals using in situ and surface-based NO_2 observations, *Atmos. Chem. Phys.*, 14, 11587–11609, https://doi.org/10.5194/acp-14-11587-2014, 2014.

Lamsal, L.N., Duncan, B.N., Yoshida, Y., Krotkov, N.A., Pickering, K.E., Streets, D.G., Lu, Z.: U.S. NO_2 trends (2005–2013): EPA Air Quality System (AQS) data versus improved observations from the Ozone Monitoring Instrument (OMI), *Atmos. Env.*, 110, pp:130-143, doi:10.1016/j.atmosenv.2015.03.055, 2015.

Laughner, J. L., Zhu, Q., and Cohen, R. C.: Evaluation of version 3.0B of the BEHR OMI NO_2 product. *Atmos. Meas. Tech.*, *12*, 129–146. https://doi.org/10.5194/amt-12-129-2019, 2019.

Laughner, J.J. and Cohen, R.C.: Direct observation of changing NO_x lifetime in North American cities, *Science,* 366, 6466, pp. 723-727, doi: 10.1126/science.aax6832, 2019.

Levelt, P. F., van den Oord, G. H. J., Dobber, M. R., Dirksen, R. J., Malkki, A., Visser, H., de Vries, J., and Stammes, P.: The ozone monitoring instrument. *IEEE Trans. Geosci. Remote Sens.*, *44*(5), 1093–1101. https://doi.org/Urn:nbn:nl:ui:25-648485, 2006.

Levelt, P. F., Joiner, J., Tamminen, J., Veefkind, J. P., Bhartia, P. K., Stein Zweers, D. C., Duncan, B. N., Streets, D. G., Eskes, H., van der A, R., McLinden, C., Fioletov, V., Carn, S., de Laat, J., DeLand, M., Marchenko, S., McPeters, R., Ziemke, J., Fu, D., Liu, X., Pickering, K., Apituley, A., González Abad, G., Arola, A., Boersma, F., Chan Miller, C., Chance, K., de Graaf, M., Hakkarainen, J., Hassinen, S., Ialongo, I., Kleipool, Q., Krotkov, N., Li, C., Lamsal, L., Newman, P., Nowlan, C., Suleiman, R., Tilstra, L. G., Torres, O., Wang, H., and Wargan, K.: The Ozone Monitoring Instrument: overview of 14 years in space, *Atmos. Chem. Phys.*, 18, 5699–5745, https://doi.org/10.5194/acp-18-5699-2018, 2018.

Lin, J.-T., Martin, R. V., Boersma, K. F., Sneep, M., Stammes, P., Spurr, R., Wang, P., Van Roozendael, M., Clémer, K., and Irie, H.: Retrieving tropospheric nitrogen dioxide from the Ozone Monitoring Instrument: effects of aerosols, surface reflectance anisotropy, and vertical profile of nitrogen dioxide, *Atmos. Chem. Phys.*, 14, 1441–1461, https://doi.org/10.5194/acp-14-1441-2014, 2014.

Lin, J.-T., Liu, M.-Y., Xin, J.-Y., Boersma, K. F., Spurr, R., Martin, R., and Zhang, Q.: Influence of aerosols and surface reflectance on satellite NO_2 retrieval: seasonal and spatial characteristics and implications for NO_x emission constraints, *Atmos. Chem. Phys.*, 15, 11217-11241, doi:10.5194/acp-15-11217-2015, 2015.

1061 Liu, F., Duncan, B. N., Krotkov, N. A., Lamsal, L. N., Beirle, S., Griffin, D., McLinden, C. A.,
1062   Goldberg, D. L., and Lu, Z.: A methodology to constrain carbon dioxide emissions from coal-
1063   fired power plants using satellite observations of co-emitted nitrogen dioxide, *Atmos. Chem.*
1064   *Phys.*, 20, 99–116, https://doi.org/10.5194/acp-20-99-2020, 2020.

1065 Liu, M.-Y., Lin, J.-T., Boersma, K. F., Pinardi, G., Wang, Y., Chimot, J., Wagner, T., Xie, P.,
1066   Eskes, H., Van Roozendael, M., Hendrick, F., Wang, P., Wang, T., Yan, Y.-Y., Chen, L.-L.,
1067   and Ni, R.-J.: Improved aerosol correction for OMI tropospheric NO_2 retrieval over East Asia:
1068   constraint from CALIOP aerosol vertical profile, *Atmos. Meas. Tech.*, 12, 1-21,
1069   doi:10.5194/amt-12-1-2019, 2019.

1070 Lu, Z., Streets, D. G., de Foy, B., Lamsal, L. N., Duncan, B. N., and Xing, J.: Emissions of nitrogen
1071   oxides from US urban areas: Estimation from Ozone Monitoring Instrument retrievals for
1072   2005-2014, *Atmos. Chem. Phys.*, *15*(18), 10367–10383. https://doi.org/10.5194/acp-15-
1073   10367-2015, 2015.

1074 Lucht, W., Schaaf, C. B., and Strahler, A. H.: An algorithm for the retrieval of albedo from space
1075   using semiempirical BRDF models, *IEEE Trans. Geosci. Remote Sens.*, 38, 977–998, 2000.

1076 Marchenko, S., Krotkov, N. A., Lamsal, L. N., Celarier, E. A., Swartz, W. H., and Bucsela, E. J.:
1077   Revising the slant column density retrieval of nitrogen dioxide observed by the Ozone
1078   Monitoring Instrument, *J. Geophys. Res.*, 120, 5670--5692, 2015.

1079 Martin, R. V., Chance, K., Jacob., D.J., Kurosu, T.P., Spurr., R.J.D., Bucsela, E., Gleason, J.F.,
1080   Palmer, P.I., Bey, I., Fiore, A.M., Li, Q., Yantosca, R.M., Koelemeijer, R.B.A.: An improved
1081   retrieval of tropospheric nitrogen dioxide from GOME, *J. Geophys. Res.*, 107, 4437,
1082   doi:10.1029/2001JD001027, 2002.

1083 McLinden, C. A., Fioletov, V. E., Boersma, K. F., Kharol, S. K., Krotkov, N., Lamsal, L., et al.:
1084   Improved satellite retrievals of NO_2 and SO_2 over the Canadian oil sands and comparisons
1085   with surface measurements. *Atmos. Chem. Phys.*, *14*, 3637–3656.
1086   https://doi.org/10.5194/acp-14-3637-2014, 2014.

1087 Mishchenko, M. I. and Travis, L. D.: Satellite retrieval of aerosol properties over the ocean using
1088   polarization as well as intensity of reflected sunlight, *J. Geophys. Res.*, 102, 16989–
1089   17013, https://doi.org/10.1029/96JD02425, 1997.

1090 Miyazaki, K., Eskes, H., Sudo, K., Boersma, K.   F., Bowman, K.,   and Kanaya, Y.: Decadal
1091   changes in global surface NO_x emissions from multi-constituent satellite data

assimilation, *Atmos. Chem. Phys.*, 2, 807–837, 10.5194/acp-17-807-2017, 2017.

Montgomery, A., and Holloway, T.: Assessing the relationship between satellite-derived NO$_2$ and economic growth over the 100 most populous global cities, *J. Appl. Rem. Sens.*, 04, 1, 10.1117/1.jrs.12.042607, 2018.

Morel, A.: Optical modeling of the upper ocean in relation to its biogeneous matter content (Case I waters), *J. Geophys. Res.,* 93, 10749–10768, https://doi.org/10.1029/JC093iC09p10749, 1988.

National Geophysical Data Center, 2006. 2-minute Gridded Global Relief Data (ETOPO2) v2. National Geophysical Data Center, NOAA. doi:10.7289/V5J1012Q [access date:2017/05/22].

Nolin, A., Armstrong, R., and Maslanik, J.: Near real-time SSM/I EASE-grid daily global ice concentration and snow extent, Digit, Media, Natl. Snow Ice Data Center, Boulder, CO, USA, 2005.

Nowlan, C. R., Martin, R.V., Philip, S., Lamsal, L.N., Krotkov, N.A., Marais, E.A., Wang, S., and Zhang, Q.: Global dry deposition of nitrogen dioxide and sulfur fioxide inferred from space-based measurements, *Global Biogeochem. Cycles,* 28, 10, doi: 10.1002/2014GB004805, 2014.

Nowlan, C. R., Liu, X., Leitch, J. W., Chance, K., González Abad, G., Liu, C., Zoogman, P., Cole, J., Delker, T., Good, W., Murcray, F., Ruppert, L., Soo, D., Follette-Cook, M. B., Janz, S. J., Kowalewski, M. G., Loughner, C. P., Pickering, K. E., Herman, J. R., Beaver, M. R., Long, R. W., Szykman, J. J., Judd, L. M., Kelley, P., Luke, W. T., Ren, X., and Al-Saadi, J. A.: Nitrogen dioxide observations from the Geostationary Trace gas and Aerosol Sensor Optimization (GeoTASO) airborne instrument: Retrieval algorithm and measurements during DISCOVER-AQ Texas 2013, *Atmos. Meas. Tech.*, 9, 2647–2668, https://doi.org/10.5194/amt-9-2647-2016, 2016.

Palmer, P. I., Jacob, D. J., Fiore, A. M., and Martin, R. V., Air mass factor formulation for spectroscopic measurements from satellites: Application to formaldehyde retrievals from the Global Ozone Monitoring Experiment, *J. Geophys. Res.*, 106, 14539–514550, https://doi.org/10.1029/2000JD900772, 2001.

Pickering, K.E., Bucsela, E., Allen, D., Ring, A., Holzworth, R., and Krotkov, N.A.: Estimates of lightning NO$_x$ production based on OMI NO$_2$ observations over the Gulf of Mexico, *J.*

Geophys. Res., 121, 14, pp 8668-8691, DOI: 10.1002/2015JD024179, 2016.

Platt, U., and Stutz, J.: Differential optical absorption spectroscopy (DOAS), principle and applications, Springer Verlag, Heidelberg, 2006.

Pope, R. J., Chipperfield, M. P., Savage, N. H., Ordóñez, C., Neal, L. S., Lee, L. A., Dhomse, S. S., Richards, N. A. D., and Keslake, T. D.: Evaluation of a regional air quality model using satellite column NO_2: treatment of observation errors and model boundary conditions and emissions, *Atmos. Chem. Phys.*, 15, 5611–5626, https://doi.org/10.5194/acp-15-5611-2015, 2015.

Qin, W., Fasnacht, Z., Haffner, D., Vasilkov, A., Joiner, J., Krotkov, N., Fisher, B., and Spurr, R.: A geometry-dependent surface Lambertian-equivalent reflectivity product for UV–Vis retrievals – Part 1: Evaluation over land surfaces using measurements from OMI at 466 nm, *Atmos. Meas. Tech.*, 12, 3997–4017, https://doi.org/10.5194/amt-12-3997-2019, 2019.

Rasool, Q. Z., Zhang, R., Lash, B., Cohan, D. S., Cooter, E. J., Bash, J. O., and Lamsal, L. N.: Enhanced representation of soil NO emissions in the Community Multiscale Air Quality (CMAQ) model version 5.0.2, *Geosci. Mod. Develop.*, 9, 3177–3197, 10.5194/gmd-9-3177-2016, 2016.

Ridley, B. A. and Grahek, F. E.: A small, low flow, high sensitivity reaction vessel for NO chemiluminescence detectors, *J. Atmos. Oceanic Technol.*, 7, 307–311, https://doi.org/10.1175/1520-0426(1990)0072.0.CO, 1990.

Rienecker, M. M., Suarez, M. J., Gelaro, R., Todling, R., Bacmeister, J., Liu, E., Bosilovich, M. G., Schubert, S. D., Takacs, L., Kim, G.-K., Bloom, S., Chen, J., Collins, D., Conaty, A., da Silva, A., Gu, W., Joiner, J., Koster, R. D., Lucchesi, R., Molod, A., Owens, T., Pawson, S., Pegion, P., Redder, C. R., Reichle, R., Robertson, F. R., Ruddick, A. G., Sienkiewicz, M., and Woollen, J.: MERRA: NASA's Modern-Era Retrospective Analysis for Research and Applications, *J. Clim.*, 24, 3624–3648, https://doi.org/10.1175/JCLI-D-11-00015.1, 2011.

Rothman, L. S., Gordon., I.E., Barbe, A., Chris Benner, D., Bernath, P.F., Birk, M., Boudon, V., Brown, L.R., Campargue, A., Champion, J.-P., Chance, K., Coudert, L.H., Dana, V., Devi, V.M., Fally, S., Flaud, J.-M., Gamache, R.R., Goldman, A., Jacquemart, D., Kleiner, I., Lacome, N., Lafferty, W.J., Mandin, J.-Y., Massie, S.T., Mikhailenko, S.N., Miller, E.E., Moazzen-Ahmad, N., Naumenko, O.V., Nikitin, A.V., Orphal, J., Perevalov, V.I., Perrin, A., Predoi-Cross, A., Rinsland, C.P., Rotger, M., Šimečková, M., Smith, M.A.H., Sung, K.,

Tashkun, S.A., Tennyson, J., Toth, R.A., Vandaele, A.C., Vander Auwera, J.: The HITRAN 2008 molecular spectroscopic database, *J. Quant. Spectrosc. Radiat. Trans.*, 114, 533– 572, 2009.

Russell, A. R., Perring, A. E., Valin, L. C., Bucsela, E. J., Browne, E. C., Wooldridge, P. J., and Cohen, R. C.: A high spatial resolution retrieval of NO_2 column densities from OMI: method and evaluation, *Atmos. Chem. Phys.*, 11, 8543–8554, https://doi.org/10.5194/acp-11-8543-2011, 2011.

Schaaf, C. B., Gao, F., Strahler, A. H., Lucht, W., Li, X., Tsang, T., Strugnell, N. C., Zhang, X., Jin, Y., Muller, J.-P., Lewis, P., Barnsley, M., Hobson, P., Disney, M., Roberts, G., Dunderdale, M., Doll, C., d'Entremont, R., Hu, B., Liang, S., and Privette, J. L.: First operational BRDF, albedo and nadir reflectance products from MODIS, *Rem. Sens. Environ.*, 83, 135–148, 2002.

Schaaf, C. L. B., Liu, J., Gao, F., and Strahler, A. H.: MODIS albedo and reflectance anisotropy products from Aqua and Terra, in: Land Remote Sensing and Global Environmental Change: NASA's Earth Observing System and the Science of ASTER and MODIS, Remote Sensing and Digital Image Processing Series, edited by: Ramachandran, B., Justice, C., and Abrams, M., Vol. 11, Springer-Verlag, New York, 873 pp., 2011.

Schenkeveld, V. M. E., Jaross, G., Marchenko, S., Haffner, D., Kleipool, Q. L., Rozemeijer, N. C., Veefkind, J. P., and Levelt, P. F.: In-flight performance of the Ozone Monitoring Instrument, *Atmos. Meas. Tech.,* 10, 1957–1986, https://doi.org/10.5194/amt-10-1957-2017, 2017.

Schreier, S. F., Richter, A., Kaiser, J. W., and Burrows, J. P.: The empirical relationship between satellite-derived tropospheric NO_2 and fire radiative power and possible implications for fire emission rates of NO_x, *Atmos. Chem. Phys.*, 5, 2447–2466, 10.5194/acp-14-2447-2014, 2014.

Shah, V., Jacob, D. J., Li, K., Silvern, R. F., Zhai, S., Liu, M., Lin, J., and Zhang, Q.: Effect of changing NO_x lifetime on the seasonality and long-term trends of satellite-observed tropospheric NO_2 columns over China, *Atmos. Chem. Phys. Disc.*, 1–23, 10.5194/acp-2019-670, 2019.

Spurr, R. J. D.: VLIDORT: a linearized pseudo-spherical vector discrete ordinate radiative transfer code for forward model and retrieval studies in multilayer multiple scattering media*, J. Quant. Spectrosc. Rad. Trans.,* 102, 316–421, https://doi.org/10.1016/j.jqsrt.2006.05.005, 2006.

1185   Stammes, P., Sneep, M., de Haan, J. F., Veefkind, J. P., Wang, P., and Levelt, P. F.: Effective
1186   cloud fractions from the Ozone Monitoring Instrument: Theoretical framework and
1187   validation, *J. Geophys. Res.,* 113, D16S38, https://doi.org/10.1029/2007JD008820, 2008.

1188   Strahan, S. E., Duncan, B.N., and Hoor, P.: Observationally derived transport diagnostics for the
1189   lowermost stratosphere and their application to the GMI chemistry and transport
1190   model, *Atmos. Chem. Phys.*, **7**, 2435– 2445, 2007.

1191   Strode, S.A., Rodriguez, J.M., Logan, J.A., Cooper, O.R., Witte, J.C., Lamsal, L.N., Damon, M.,
1192   Van Aartsen, B., Steenrod, S.D., and Strahan, S.E.:Trends and variability in surface ozone
1193   over the United States, *J. Geophys. Res.*, doi: 10.1002/2014JD022784, 2015.

1194   Tang, W., Cohan, D.   S., Pour-Biazar, A., Lamsal, L.   N., White, A.
1195   T., Xiao, X., Zhou, W., Henderson, B. H., and Lash, B. F.: Influence of satellite-derived
1196   photolysis rates and NO_x emissions on Texas ozone modeling, *Atmos. Chem. Phys.*, 4, 1601–
1197   1619, 10.5194/acp-15-1601-2015, 2015.

1198   Thalman, R., and Volkamer, R.: Temperature dependent absorption cross-sections of O_2-O_2
1199   collision pairs between 340 and 630 nm and at atmospherically relevant pressure, *Phys.*
1200   *Chem. Chem. Phys.*, 15, 15371–15381, https://doi.org/10.1039/C3CP50968K, 2013.

1201   Thornton, J. A., Wooldridge, P. J., and Cohen, R. C.: Atmospheric NO_2: in situ laser-induced
1202   fluorescence detection at parts per trillion mixing ratios, *Anal. Chem.*, 72, 528–539,
1203   https://doi.org/10.1021/ac9908905, https://doi.org/10.1021/ac9908905, 2000.

1204   Tong, D., Lamsal, L.N., Pan, L., Kim, H., Lee, P., Chai, T., Pickering, K.E.: Long-term NO_x trends
1205   over large cities in the United States during the Great Recession: Intercomparison of satellite
1206   retrievals, ground observations, and emission inventories, *Atmos. Env.,* 109, doi:
1207   10.1016/j.atmosenv.2015.01.035, 2015.

1208   Torres, O., Tanskanen, A., Veihelman, B., Ahn, C., Braak, R., Bhartia, P. K., Veefkind, V., and
1209   Levelt, P.: Aerosols and Surface UV Products from OMI Observations: An Overview, *J.*
1210   *Geophys. Res.*, 112, D24S47, https://doi.org/10.1029/2007JD008809, 2007.

1211   van der A, R. J., Eskes, H.J., Boersma, K.F., van Noije, T.P.C., Van Roozendael, M., De Smedt, I.,
1212   Peters, D. H. M. U., and Meijer E.W.: Identification of NO_2 sources and their trends from
1213   space using seasonal variability analyses, *J. Geophys. Res.*, 113, D04302,
1214   doi:10.1029/2007JD009021, 2008.

1215   van Geffen, J. H. G. M., Boersma, K. F., Van Roozendael, M., Hendrick, F., Mahieu, E., De Smedt,

1216   I., Sneep, M., and Veefkind, J. P.: Improved spectral fitting of nitrogen dioxide from OMI in
1217   the 405–465 nm window, *Atmos. Meas. Tech.*, 8, 1685–1699, https://doi.org/10.5194/amt-8-
1218   1685-2015, 2015.

1219   Vandaele, A. C., Hermans, C., Simon, P.C., Carleer, M., Colin, R., Fally, S., Mérienne, M.F.,
1220   Jenouvrier, A., and Coquart, B.: Measurements of the NO_2 absorption cross-section from
1221   42,000 cm^{-1} to 10,000 cm^{-1} (238-1000 nm) at 220 K and 294 K, *J. Quant. Spectrosc. Radiat.*
1222   *Trans.*, 59, 171– 184, 1998.

1223   Vasilkov, A., Joiner, J., Gleason, J., and Bhartia, P.K.: Ocean Raman scattering in satellite
1224   backscatter UV measurements, *Geophys. Res. Lett.*, 29, 1837, doi:10.1029/2002GL014955,
1225   2002.

1226   Vasilkov, A. P., Herman, J. R., Ahmad, Z., Karu, M., and Mitchell, B. G.: Assessment of the
1227   ultraviolet radiation field in ocean waters from space-based measurements and full radiative-
1228   transfer calculations, *Appl. Opt.,* 44, 2863–2869, https://doi.org/10.1364/AO.44.002863,
1229   2005.

1230   Vasilkov, A.P., Joiner, J., Spurr, R., Bhartia, P.K., Levelt, P., Stephens, G.: Evaluation of the OMI
1231   cloud pressures derived from rotational Raman scattering by comparisons with other satellite
1232   data and radiative transfer simulations, *J. Geophys. Res.*, 113, d15,
1233   https://doi.org/10.1029/2007JD008689, 2008.

1234   Vasilkov, A. P., Joiner, J., Haffner, D., Bhartia, P. K., and Spurr, R. J. D.: What do satellite
1235   backscatter ultraviolet and visible spectrometers see over snow and ice? A study of clouds
1236   and ozone using the A-train, *Atmos. Meas. Tech.*, 3, 619–629, https://doi.org/10.5194/amt-3-
1237   619-2010, 2010.

1238   Vasilkov, A., Qin, W., Krotkov, N., Lamsal, L., Spurr, R., Haffner, D., Joiner, J., Yang, E.-S., and
1239   Marchenko, S.: Accounting for the effects of surface BRDF on satellite cloud and trace-gas
1240   re- trievals: a new approach based on geometry-dependent Lambertian equivalent
1241   reflectivity applied to OMI algorithms, *Atmos. Meas. Tech.*, 10, 333–349,
1242   https://doi.org/10.5194/amt-10-333-2017, 2017.

1243   Vasilkov, A., Yang, E.-S., Marchenko, S., Qin, W., Lamsal, L., Joiner, J., Krotkov, N., Haffner,
1244   D., Bhartia, P.K., Spurr, R.: A cloud algorithm based on the O_2-O_2 477 nm absorption band
1245   featuring an advanced spectral fitting method and the use of surface geometry-dependent
1246   Lambertian-equivalent reflectivity, *Atmos. Meas. Tech.*, 11, 4093-4107, doi: 10.5194/amt-11-

1247   4093-2018, 2018.

1248 Vasilkov, A., Krotkov, N., Yang, E.-S., Lamsal, L., Joiner, J., Castellanos, P., Fasnacht, Z., and

1249   Spurr, R.: Explicit and consistent aerosol correction for visible wavelength satellite cloud and

1250   nitrogen dioxide retrievals based on optical properties from a global aerosol analysis, *Atmos.*

1251   *Meas. Tech. Discuss.*, https://doi.org/10.5194/amt-2019-458, in review, 2020.

1252 Veefkind J. P., de Haan, J. F., Brinksma, E. J., Kroon, M., and Levelt, P. F.: Total ozone from the

1253   Ozone Monitoring Instrument (OMI) using the DOAS technique, *IEEE Trans. Geophys.*

1254   *Remote Sens.*, 44, 1239–1244, 2006.

1255 Veefkind, J. P., de Haan, J. F., Sneep, M., and Levelt, P. F.: Improvements to the OMI O_2–

1256 O_2 operational cloud algorithm and comparisons with ground-based radar–lidar observations,

1257   *Atmos. Meas. Tech.*, 9, 6035–6049, https://doi.org/10.5194/amt-9-6035-2016, 2016.

1258 Vinken, G. C. M., Boersma, K. F., Donkelaar, A., and Zhang, L., Constraints on ship NO_x

1259   emissions in Europe using GEOS-Chem and OMI satellite NO_2 observations, *Atmos. Chem.*

1260   *Phys.*, 3, 1353–1369, 10.5194/acp-14-1353-2014, 2014a.

1261 Vinken, G. C. M., Boersma, K. F., Maasakkers, J. D., Adon, M., and Martin, R. V.: Worldwide

1262   biogenic soil NO_x emissions inferred from OMI NO_2 observations, *Atmos. Chem. Phys.*, 18,

1263   10363–10381, 10.5194/acp-14-10363-2014, 2014b.

1264 Volkamer, R., Spietz, P., Burrows, J.P., and Platt, U., High-resolution absorption cross-section of

1265   Glyoxal in the UV/VIS and IR spectral ranges, *J. Photochem. Photobiol.*, **172**, 35– 46,

1266   doi:10.1016/j.jphotochem.2004.11.011, 2005.

1267 Meissner, T. and Wentz, F.J.: The Complex Dielectric Constant of Pure and Sea Water from

1268   Microwave Satellite Observations. *IEEE Trans. Geo. Rem. Sens.*, 42, 1836-1849.

1269   http://dx.doi.org/10.1109/TGRS.2004.831888, 2004.

1270 Wentz, F., Hilburn, K., and Smith, K.: RSS SSMIS ocean product grids daily from DMSP F16

1271   NETCDF. Dataset available online from the NASA Global Hydrology Resource Center

1272   DAAC, Huntsville, Alabama, USA, https://doi.org/10.5067/MEASURES/DMSP-

1273   F16/SSMIS/DATA301, 2012.

1274 Zara, M., Boersma, K. F., De Smedt, I., Richter, A., Peters, E., van Geffen, J. H. G. M., Beirle, S.,

1275   Wagner, T., Van Roozendael, M., Marchenko, S., Lamsal, L. N., and Eskes, H. J.: Improved

1276   slant column density retrieval of nitrogen dioxide and formaldehyde for OMI and GOME-2A

1277   from QA4ECV: intercomparison, uncertainty characterisation, and trends, *Atmos. Meas.*

1278   *Tech.*, 11, 4033–4058, https://doi.org/10.5194/amt-11-4033-2018, 2018.

1279   Zhou, Y., Brunner, D., Spurr, R. J. D., Boersma, K. F., Sneep, M., Popp, C., and Buchmann, B.:

1280   Accounting for surface reflectance anisotropy in satellite retrievals of tropospheric NO_2,

1281   *Atmos. Meas. Tech.*, 3, 1185–1203, https://doi.org/10.5194/amt-3-1185-2010, 2010.

1282   Zhou, Y., Brunner, D., Hueglin, C., Henne, S., and Staehelin, J.: Changes in OMI tropospheric

1283 NO_2 columns over Europe from 2004 to 2009 and the influence of meteorological

1284   variability, *Atmos. Environ.*, 482–495, 10.1016/j.atmosenv.2011.09.024, 2012.
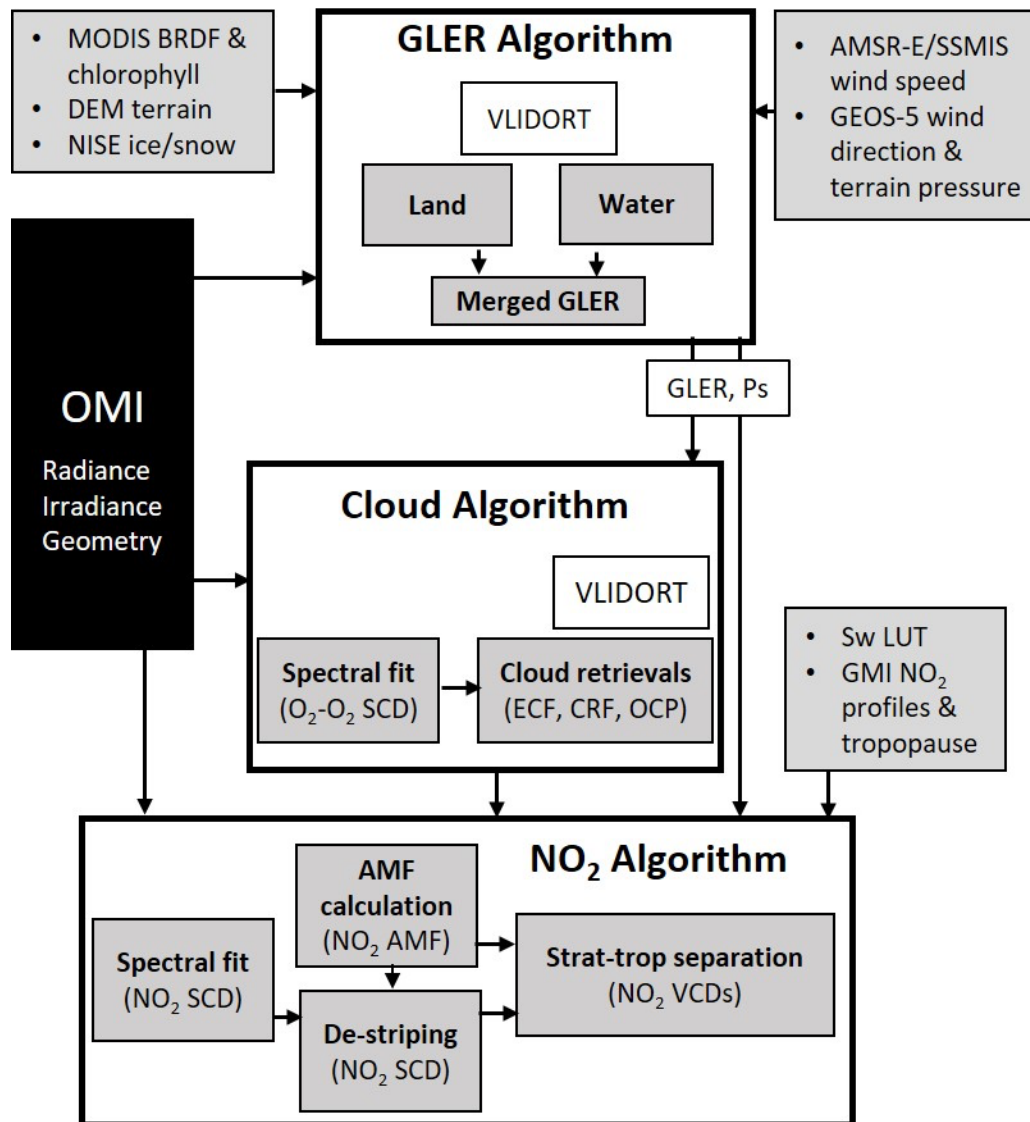
1285

1286 **Figure 1:** Schematic diagram of the NASA OMI NO_2 algorithm, version 4.0, which is coupled
1287 with the cloud and geometry-dependent surface Lambertian Equivalent Reflectivity (GLER)
1288 algorithms that ultimately produces stratospheric (strat) and tropospheric (trop) NO_2 vertical
1289 column densities (VCDs). Acronyms used here are described in relevant sections below.
1290 VLIDORT: Vector Linearized Discrete Ordinate Radiative Transfer; MODIS: Moderate

1291 Resolution Imaging Spectro-radiometer; BRDF: bidirectional reflectance distribution function;
1292 DEM: Digital Elevation Model; NISE: Near-real-time Ice and Snow Extent; AMSR-E: Advanced
1293 Microwave Scanning Radiometer for Earth Observing System (EOS); SSMIS: Special Sensor
1294 Microwave Imager / Sounder; GEOS-5: Goddard Earth Observing System, Version 5; Ps: surface
1295 (terrain) pressure over OMI pixel; ECF: Effective Cloud Fraction; CRF: Cloud Radiance Fraction;
1296 OCP: Optical Centroid Pressure; Sw: Scattering weight; LUT: Look-up table GMI: Global
1297 Modeling Initiative; AMF: Air Mass Factor; SCD: Slant Column Density.
1298
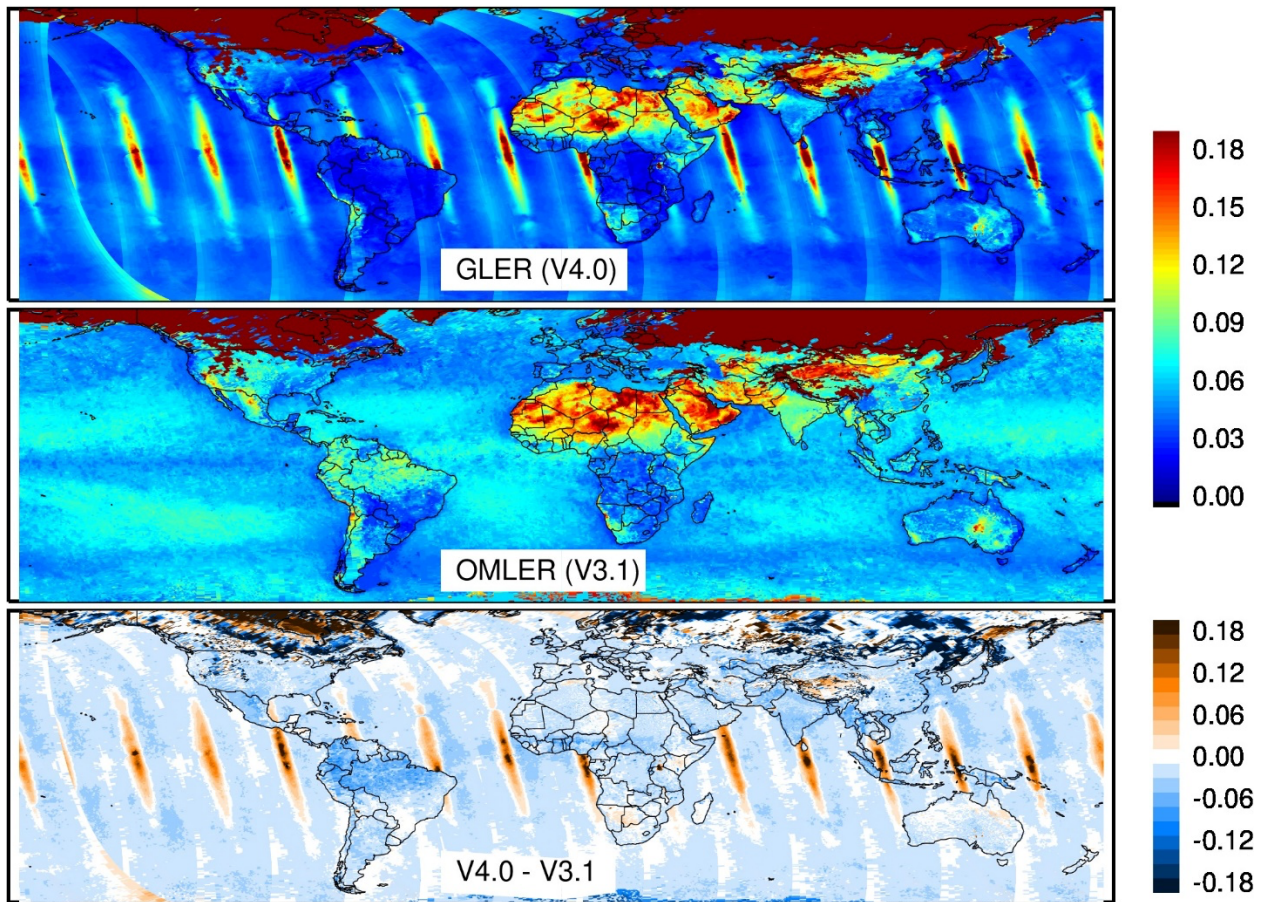
1300 **Figure 2**: Surface reflectivity at 440 nm (top) derived using MODIS BRDF data with OMI
1301 geometry (GLER) on March 20, 2005 compared with (middle) OMI-based monthly LER
1302 climatology (OMLER) for the month of March (Kleipool et al., 2008). The bottom panel shows
1303 the difference between MODIS-based and climatological surface reflectivity data.
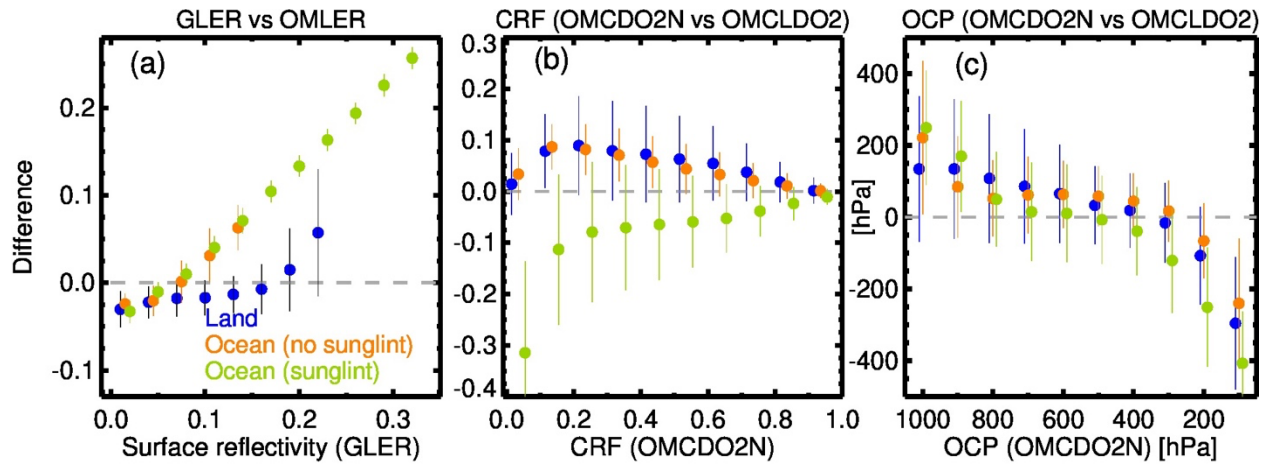
1304

Figure 3: Differences (V4.0 – V3.1) in (a) surface reflectivity, (b) cloud radiance fraction, and (c) cloud optical centroid pressure for March 20, 2005, as used in V3.1 and V4.0 algorithms and binned by the values of corresponding parameters from V4.0. Data are separated for land (blue) and ocean surfaces, and by sunglint (green) and non-sunglint (orange) geometry over ocean. The vertical bars represent the standard deviation for each bin of those parameters.

1310
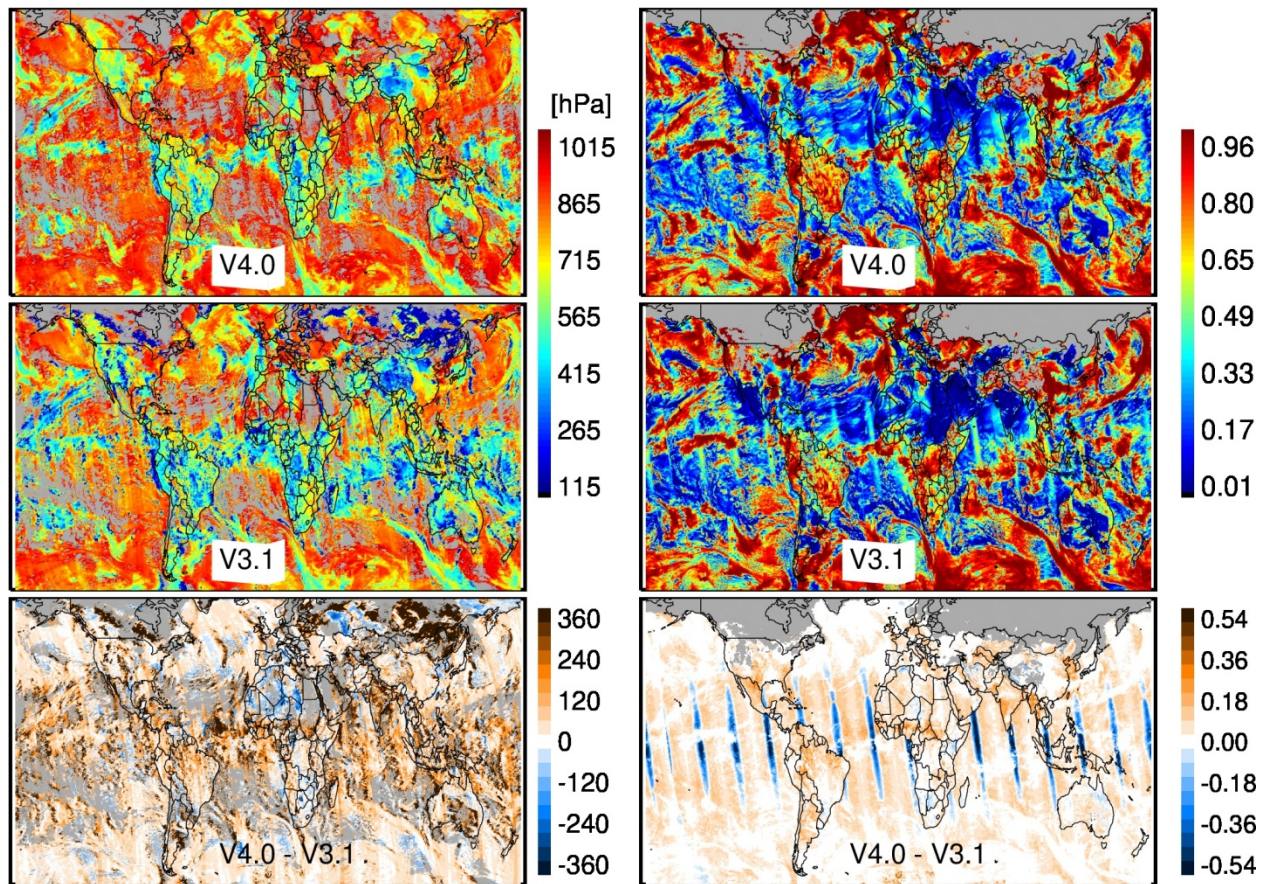
Figure 4: Cloud optical centroid pressure at 477 nm (left) and cloud radiance fraction at 440 nm (right) retrieved for March 20, 2005 with OMNO2 V4.0 (top) and V3.1 (middle) algorithms, respectively. The bottom rows show their differences. The gray color represents the OMI pixels with retrieved cloud pressure equal to terrain pressure in V4.0 on the left and over snow/ice surface identified by the NISE flag on the right.
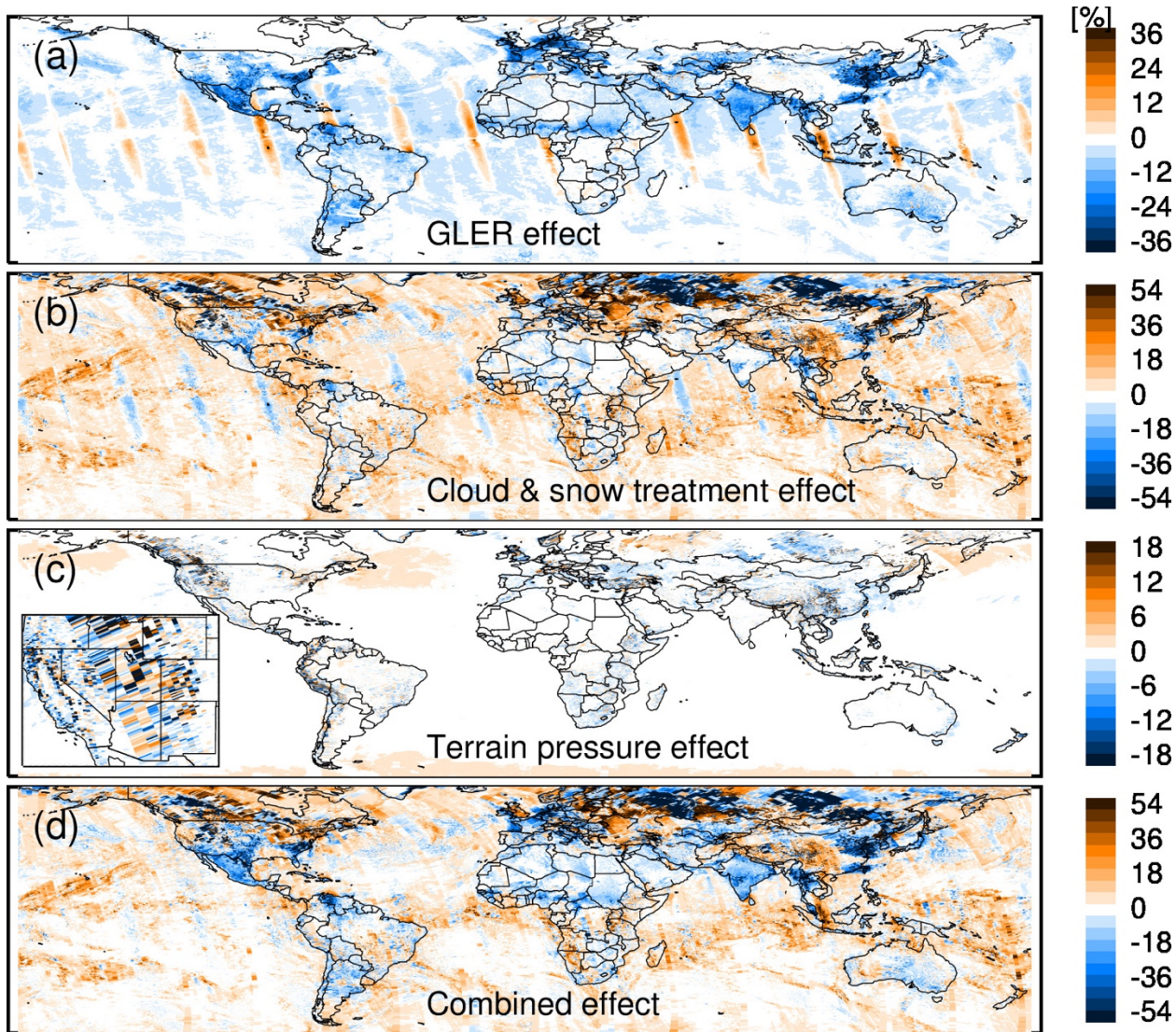
1317

1318 **Figure 5**: Impact on tropospheric AMF (i.e., V4.0 – V3.1) from changes in (a) surface reflectivity,

1319 (b) cloud and surface treatment, (c) terrain pressure, and (d) their combination on March 20, 2005.

1320 The figure 5(c) inset shows zoomed view of impact over complex terrain in the western US.
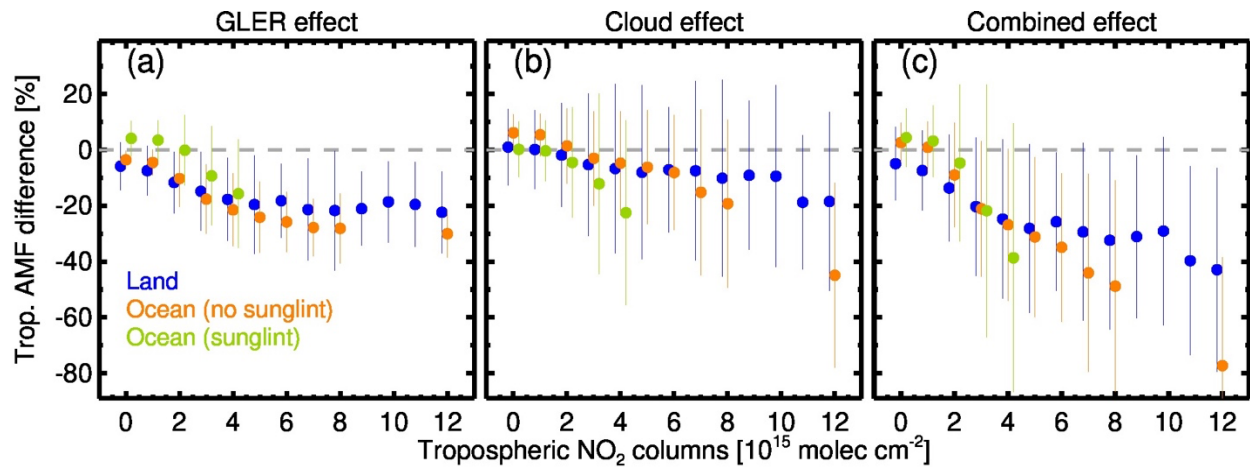
1321

Figure 6: The impact on tropospheric AMF (i.e., V4.0 – V3.1) from changes in (a) surface reflectivity, (b) cloud, and (c) their combination for clear and partially cloudy scenes (CRF<0.5) on March 20, 2005. Percent differences in tropospheric AMF are sorted by tropospheric NO_2 columns, separating them by land (blue) and ocean, and by sunglint (green) and non-sunglint (orange) geometry over ocean. The vertical bars represent the standard deviations for the tropospheric NO_2 column bins.
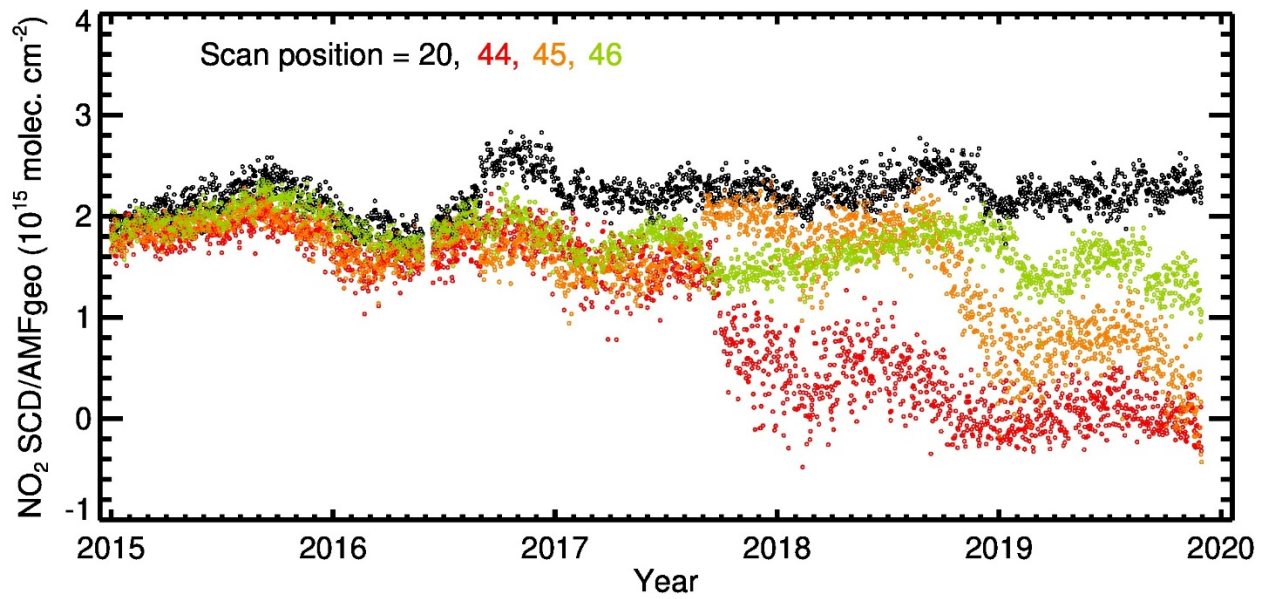
1332

1333 **Figure 7**: The time series of OMI NO_2 SCD normalized by the geometric AMF for clear-sky and

1334 partially cloudy conditions (CRF<0.5) over the Pacific Ocean. The data are separated by cross-

1335 track scan position, comparing the presumably RA-free row 20 (black) with rows 44 (red), 45

1336 (orange), and 46 (green). The row numbers are 0-based.

1337
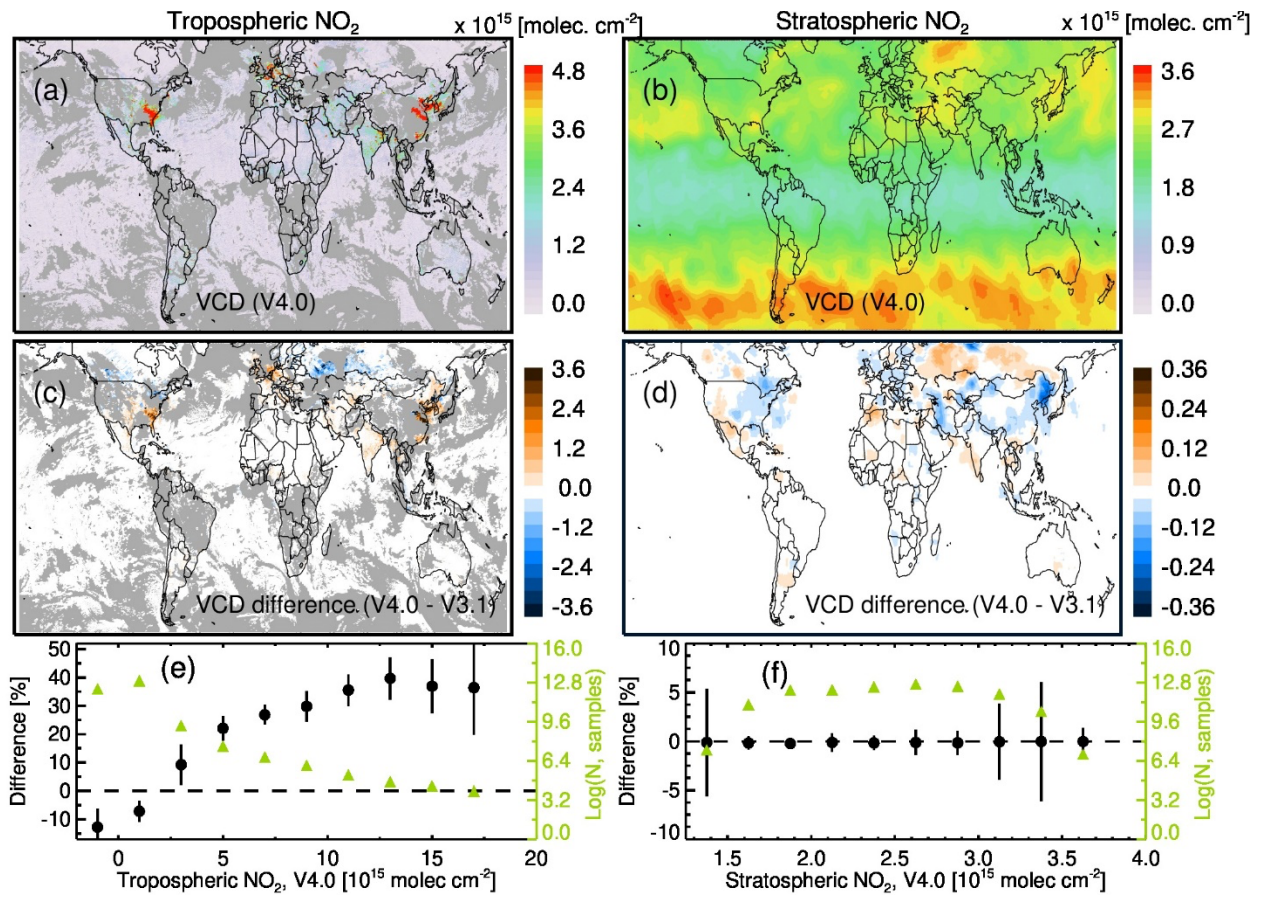
Figure 8: Tropospheric (a) and stratospheric (b) NO$_2$ VCD from V4.0 and their differences (c, d) with V3.1 data (V4.0 – V3.1) for March 20, 2005. The gray color in the tropospheric NO$_2$ maps represent cloudy areas (CRF>0.5). Bottom panels show average (black circles) and standard error (vertical bars) of the relative difference, $100 \times$ (V4.0 – V3.1)/V3.1, for tropospheric (e) and stratospheric (f) NO$_2$ VCDs plotted as a function of respective NO$_2$ column amounts. The green symbols represent the logarithm of the number of samples.
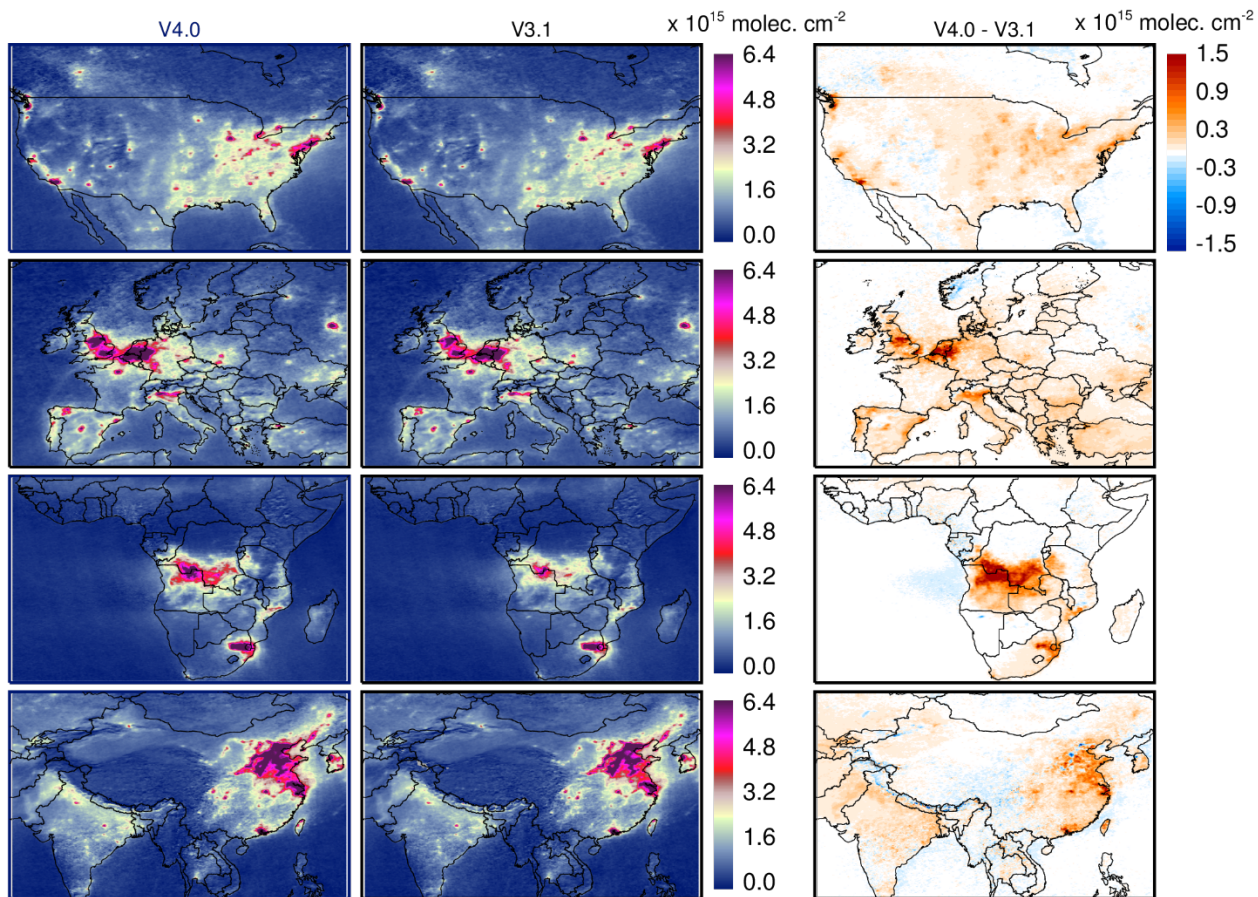
Figure 9: Three-month (June, July, August) average tropospheric NO_2 columns for low cloud conditions (CRF<0.5) in 2005 over North America (1st row), Europe (2nd row), southern Africa (3rd row), and Asia (4th row) from V4.0 (1st column), V3.1 (2nd column), and their difference (V4.0 – V3.1).
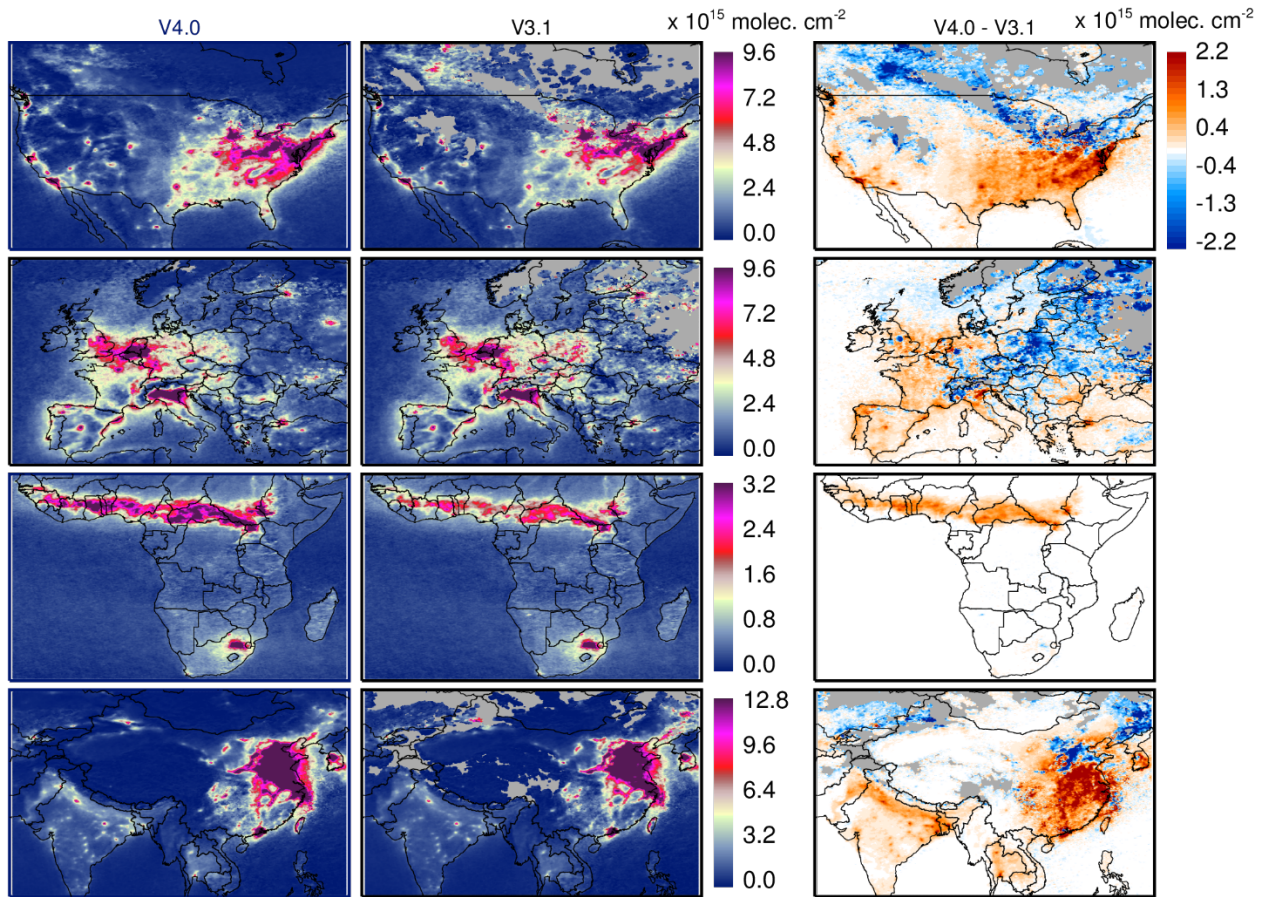
1350

Figure 10: Same as Figure 9, but for December, January, and February. The gray areas represent a lack of good observations as determined by data quality flags.

1351

1352

1353

1354

1355

1356

1357

1358

1359

1360

1361

1362

1363

1364

1365
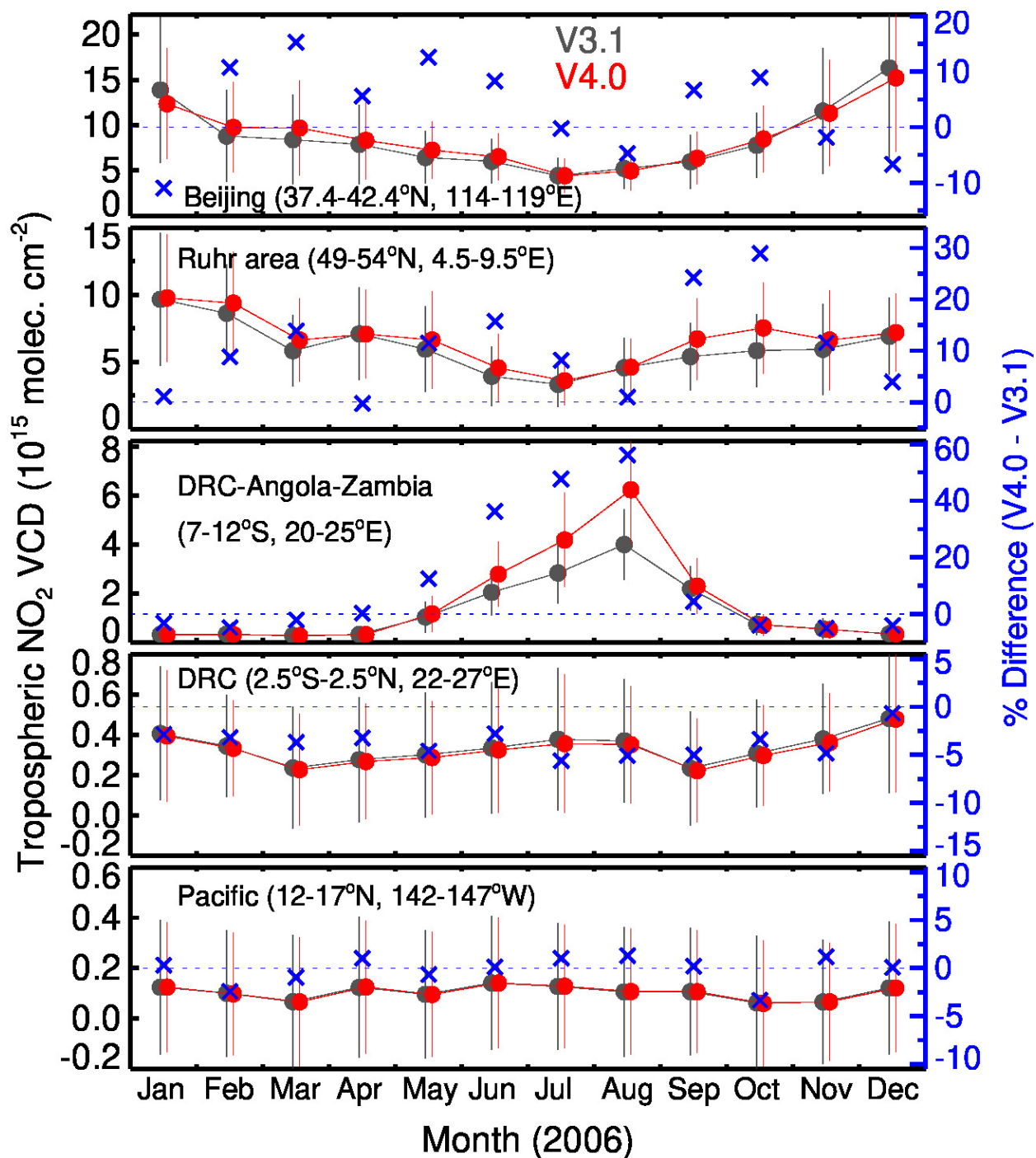
1366

1367 **Figure 11**: Monthly average tropospheric NO_2 columns in 2006 calculated from V3.1 (black)

1368 and V4.0 (red) data over selected 5° latitude × 5° longitude boxes from locations that are

1369 dominated by either anthropogenic (Beijing, China and Ruhr area, Germany), biomass burning

1370 (Democratic Republic of Congo (DRC), Angola, and Zambia), lightning (DRC), or no significant

1371 (Pacific) NO_x sources. The vertical bars show the monthly standard deviation. The blue symbols

1372   that correspond to the right y-axis show monthly relative difference (in percent) between V4.0

1373   and V3.1.
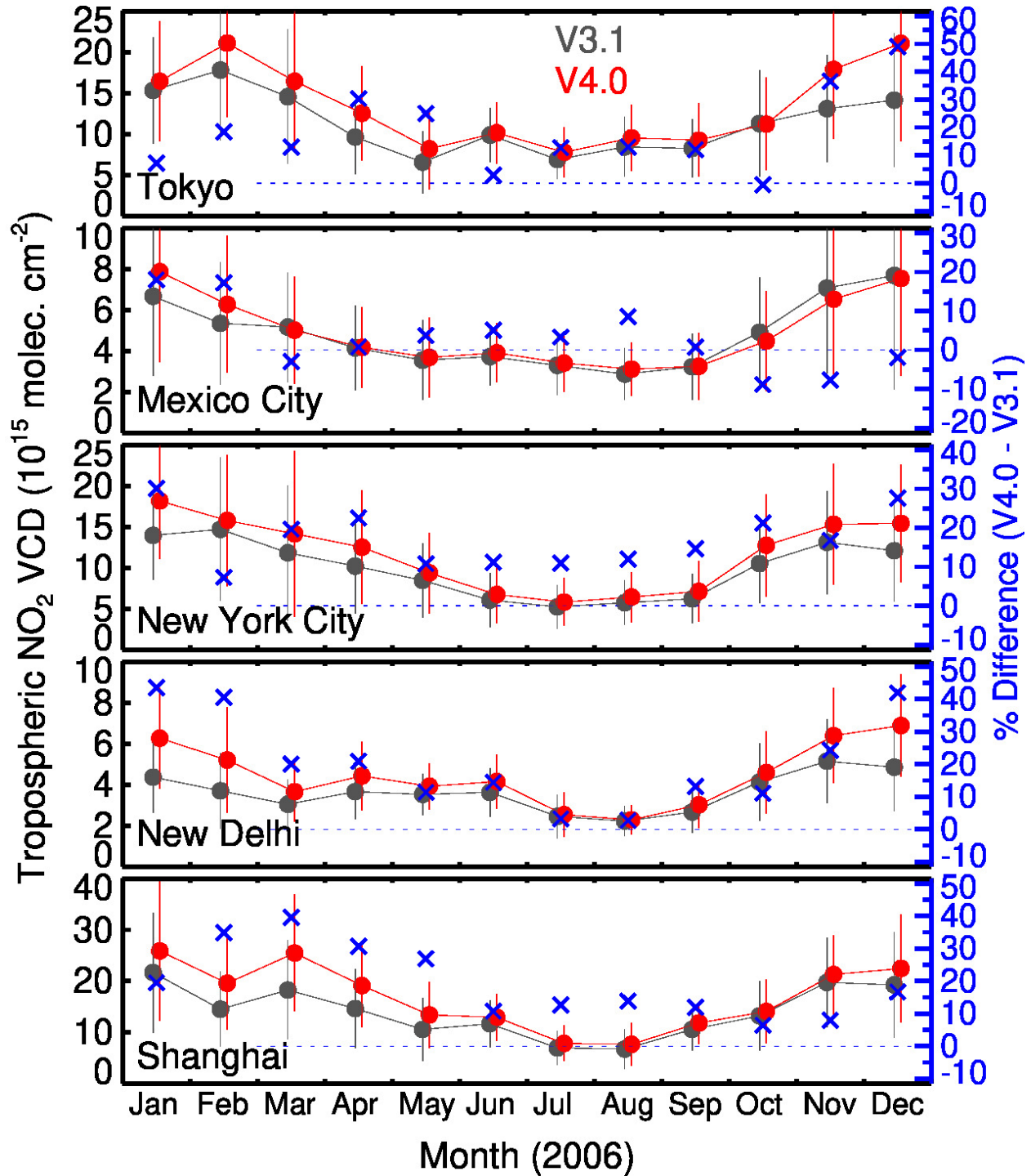
1374

1375   **Figure 12**: Same as Figure 11, but for 1º latitude × 1º longitude wide box over the five highly

1376   populated and polluted cities.

1377

1378

1379
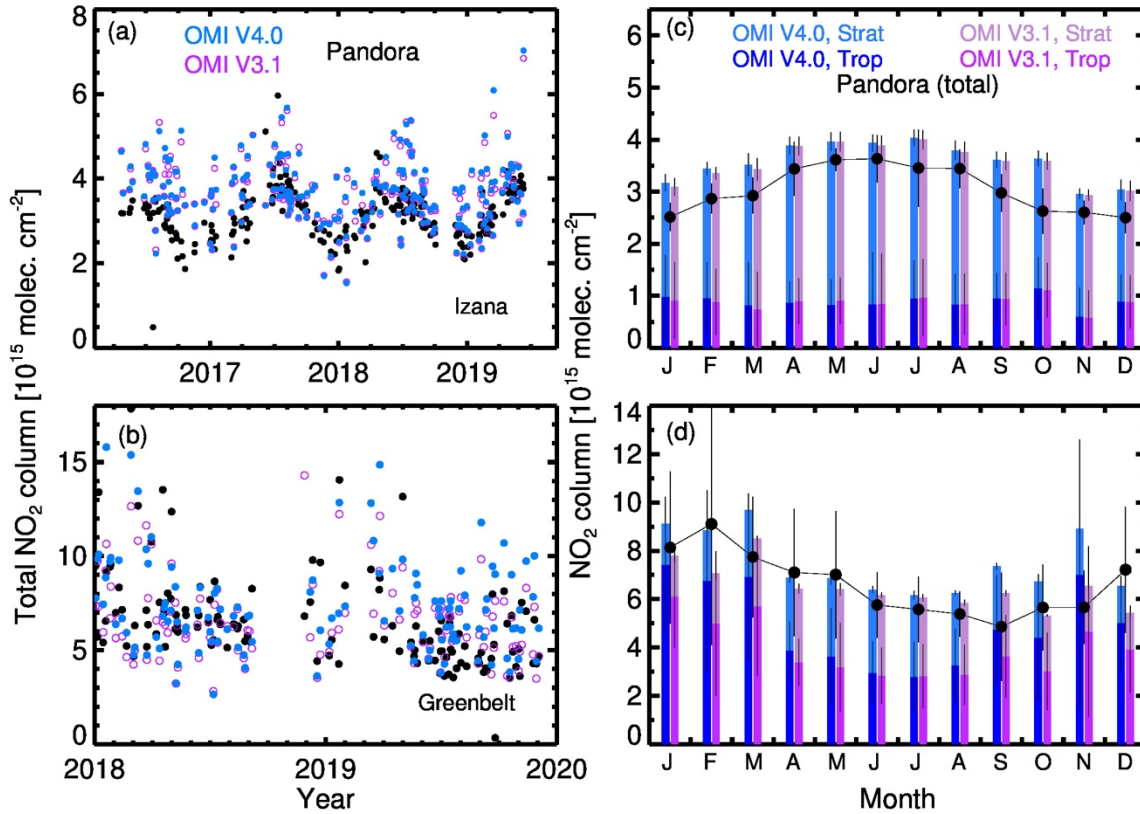
1380

1381 **Figure 13**: The time series of NO₂ total columns retrieved from Pandora (black circles) and OMI

1382 at (a) Izaña, Spain and (b) Greenbelt, Maryland, USA, with the OMI retrievals represented by the

1383 filled blue (V4.0) and open purple (V3.1) circles. Right panels show monthly variation of NO₂

1384 total columns at (c) Izaña for 2016–2019 and (d) Greenbelt for 2018-2019, as calculated from

1385 Pandora (black line with filled circles) and OMI measurements (bars). OMI NO₂ total columns

1386 retrieved with V4.0 (blue) and V3.1 (purple) are separated into tropospheric and stratospheric

1387 components. The vertical lines represent the standard deviation from the average.

1388
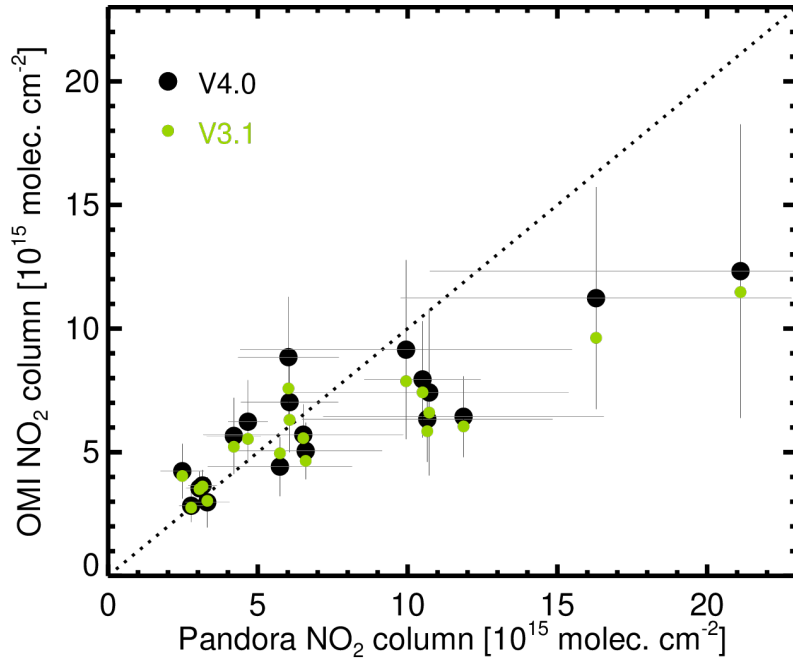
1389

1390 **Figure 14**: The scatter plot of Pandora versus OMI V4.0 (black) and V3.1 (green) average total

1391 column NO_2 for 18 Pandora sites. The vertical and horizontal lines represent the standard

1392 deviations for Pandora and OMI, respectively. The dotted line represents the 1:1 relationship.

1393
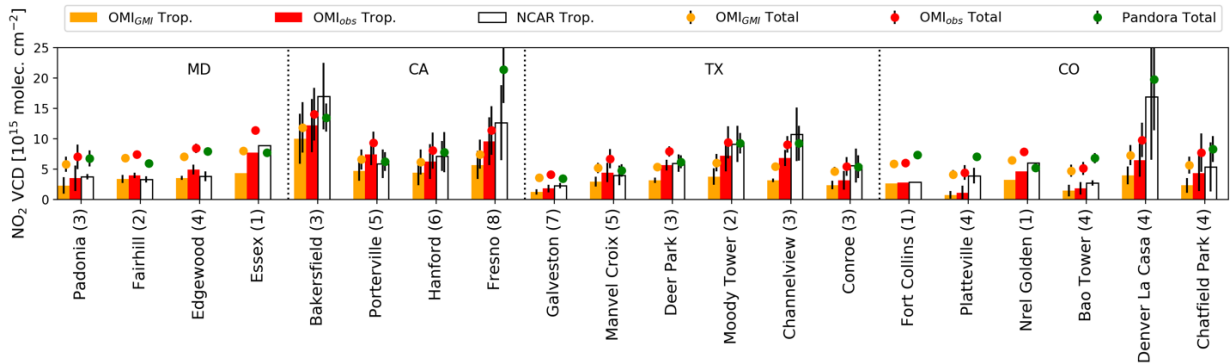
1394

1395 **Figure 15**: Site average total (circles) and tropospheric (bars) NO_2 column data from P-3B spiral

1396 (white bars), Pandora (green circles), and OMI (orange and red). The OMI tropospheric columns

1397   are derived using GMI-simulated (OMI_{GMI}, orange) and P-3B (OMI_{obs}, red) NO_2 profiles. The

1398   vertical bars for sites with over 2 observations represent the standard deviations.

1399

1400   **Table 1**. Summary of algorithms and approaches used in the NASA NO_2 algorithms versions 3.1 and 4.0

Algorithm Component		Version 3.1 (Released 2018)	Version 4.0 (Released 2019)
Spectral fit	NO_2	Modified DOAS fit (Marchenko et al, 2015)	Same as in V3.1
	O_2-O_2	DOAS fit from KNMI (Veefkind et al, 2016)	Modified DOAS fit (Vasilkov et al, 2018)
AMF	Terrain reflectivity	Monthly climatology (Kleipool et al., 2008)	Daily GLER data (Vasilkov et al., 2017; Qin et al., 2019; Fasnacht et al., 2019)
	Terrain pressure	At pixel center (calculated from terrain height and GMI terrain pressure)	Average over pixel (calculated from terrain height and GMI terrain pressure)
	Cloud pressure and fraction	Operational O_2-O_2 cloud product (OMCLDO2) v2.0 (Veefkind et al., 2016)	New O_2-O_2 cloud product (OMCDO2N) derived using the GLER product (Vasilkov et al., 2018)
	Cloud radiance fraction	Calculated at 440 nm from OMCLDO2 v2.0 cloud fraction using VLIDORT-based look-up-table	Calculated at 440 nm from OMCDO2N cloud fraction using VLIDORT-based look-up-table
	Scattering weights	TOMRAD-based look-up table	Same as in V3.1
	A-priori NO_2 profiles	GMI-derived yearly varying monthly mean profiles at 1°×1.25°	Same as in V3.1
Stripe correction		Based on data from 30°S - 5°N of 5 orbits	Same as in V3.1
Stratosphere-troposphere separation		Spatial filtering and interpolation (Bucsela et al., 2013), but with minor changes in box sizes	Same as in V3.1

1401

1402

1403

1404

1405

Table 2: Comparison of OMI V3.1 and V4.0 NO_2 retrievals based on a priori NO_2 profiles from GMI (OMI) and P-3B aircraft observations (OMI_{obs}) with P-3B observations during the DISCOVER-AQ field campaign. Shown here are correlation coefficient (r) and mean difference, which is calculated as OMI minus validation data.

Campaign locations	V3.1				V4.0			
	OMI vs P-3B		OMI_{obs} vs P-3B		OMI vs P-3B		OMI_{obs} vs P-3B	
	Mean diff. (%)	r	Mean diff. (%)	r	Mean diff. (%)	r	Mean diff. (%)	r
Maryland	-40.7	0.39	-23.7	0.61	-33.9	0.40	-5.0	0.69
California	-53.8	0.77	-42.4	0.73	-44.6	0.81	-18.7	0.83
Texas	-54.9	0.65	-25.5	0.82	-53.7	0.68	-18.8	0.85
Colorado	-67.5	0.73	-54.2	0.70	-66.2	0.70	-45.4	0.70
All	-55.5	0.75	-38.8	0.74	-50.3	0.74	-23.1	0.79

Table 3: Same as Table 2, but with Pandora NO_2 column observations.

Campaign locations	V3.1				V4.0			
	OMI vs Pandora		OMI_{obs} vs Pandora		OMI vs Pandora		OMI_{obs} vs Pandora	
	Mean diff. (%)	r	Mean diff. (%)	r	Mean diff. (%)	r	Mean diff. (%)	r
Maryland	-21.8	0.21	2.4	0.30	-13.0	0.13	25.6	0.27
California	-58.5	0.24	-47.9	0.20	-49.8	0.33	-24.6	0.49
Texas	-26.9	0.65	21.6	0.81	-25.3	0.67	31.7	0.81
Colorado	-68.2	0.72	-55.2	0.69	-67.6	0.70	-46.7	0.65
All	-52.3	0.53	-33.5	0.47	-46.9	0.56	-16.3	0.63